Sea-Ice Detection from RADARSAT Images by Gamma-based Bilateral Filtering

by

Si Xie

A thesis

presented to the University of Waterloo

in fulfillment of the

thesis requirement for the degree of

Master of Science

in

Geography

Waterloo, Ontario, Canada, 2012

Declaration

I hereby declare that I am the sole author of this thesis. This is a true copy of the thesis, including any required final revisions, as accepted by my examiners. I understand that my thesis may be made electronically available to the public.

Abstract

Spaceborne Synthetic Aperture Radar (SAR) is commonly considered a powerful sensor to detect sea ice. Unfortunately, the sea-ice types in SAR images are difficult to be interpreted due to speckle noise. SAR image denoising therefore becomes a critical step of SAR sea-ice image processing and analysis. In this study, a two-phase approach is designed and implemented for SAR sea-ice image segmentation. In the first phase, a Gamma-based bilateral filter is introduced and applied for SAR image denoising in the local domain. It not only perfectly inherits the conventional bilateral filter with the capacity of smoothing SAR sea-ice imagery while preserving edges, but also enhances it based on the homogeneity in local areas and Gamma distribution of speckle noise. The Gamma-based bilateral filter outperforms other widely used filters, such as Frost filter and the conventional bilateral filter. In the second phase, the K-means clustering algorithm, whose initial centroids are optimized, is adopted in order to obtain better segmentation results. The proposed approach is tested using both simulated and real SAR images, compared with several existing algorithms including K-means, K-means based on the Frost filtered images, and K-means based on the conventional bilateral filtered images. The F1 scores of the simulated results demonstrate the effectiveness and robustness of the proposed approach whose overall accuracies maintain higher than 90% as variances of noise range from 0.1 to 0.5. For the real SAR images, the proposed approach outperforms others with average overall accuracy of 95%.

Acknowledgements

I would like to thank my supervisor, Professor Jonathan Li, for his invaluable guidance, support and advice as I completed this work. I would also like to thank my readers, Dr. Alexander Brenning and Dr. Alexander Wong, for reviewing this thesis. Thanks also go to Dr. Su-Yin Tan for her service on the Thesis Committee.

I must also acknowledge the assistance that Tae-Jung Kwon has provided. His understanding of the image segmentation algorithms has been essential for the completion of my thesis.

The assistance of Yuanming Shu and Linlin Xu, who shared the idea of SAR image segmentation and gave me useful advice, also should be acknowledged.

I must thank my parents who have been supporting my study. They never stop caring my life and study although they have a long distance to me. I just want to say: “Thank you so much!”

The RADARSAT-2 images used in this thesis were kindly provided by the Canadian Ice Service (CIS), Environment Canada. Thanks!

Table of Contents

List of Figures

List of Tables

List of Acronyms

ANN	Artificial Neural Network
BF	bilateral filter
CBF	conventional bilateral filter
CBFK	conventional bilateral filtering followed by K-means clustering
CIS	Canadian Ice Service
ENL	equivalent number of looks
EPI	edge preserving index
ES	Expert System
ESI	edge save index
ETVOS	Extended Total Variation Optimization Segmentation
FK	Frost filtering followed by K-means clustering
GBF	Gamma-based bilateral filter
GBFK	Gamma-based bilateral filtering followed by K-means clustering
GIEP	graduated increased edge penalty
GLCM	gray level co-occurrence matrix
GLCP	gray level co-occurrence probability
GMM	Gaussian Mixture Model
KIF	K-means iterative Fisher
MRF	Markov Random Field
R1	Region 1

R2	Region 2
R3	Region 3
R4	Region 4
SAR	Synthetic Aperture Radar
SNR	Signal-to-noise ratio
WMO	World Meteorological Organization

Chapter 1

Introduction

1.1 Importance of Sea-Ice Detection

Sea ice is frozen water, which is a part of the cryosphere. The growth and decay of sea ice occur as a seasonal circulation at the surface of the ocean (Sandven and Johannessen, 2006). According to Casey (2010), Earth's climate system, oceanic surface heat and salinity fluxes, and human activities are deeply affected by sea ice processes. To this end, monitoring and mapping sea ice coverage and its dynamic changes is of importance for many countries (Sandven and Johannessen, 2006).

Sea ice has a great influence on Earth's climate system. The most important point is the albedo because sea ice has much greater albedo than sea water. As a result, more incoming solar radiation will be reflected where ice covers (Sandven and Johannessen, 2006; Casey, 2010). The difference amount of refection of solar radiation in different regions can lead to local climate change (i.e. wind). In addition, there exists an ice-albedo feedback in ice-covered area. Cooling tends to increase ice extent and hence the albedo, reducing the amount of solar energy absorbed and leading to more cooling; conversely, warming does in an inverse way (Deser et al., 2000). This feedback mechanism has mostly been discussed in terms of climate change in the

Arctic (Archer and Bufett, 2005; Eisenman and Wettlaufer, 2009). In recent years, investigating the climate change in the Arctic becomes a trend (Serreze et al., 2009).

Moreover, sea ice is also critical for the sea current. As the intermediate layer between sea water and atmosphere, sea ice prevents sea water from heated by the sun while decreases the amount of heat loss from sea water. In addition, where ice forms, the salinity of water will increase as large amount of brine will get away from ice crystals. In general, the heat and salinity fluxes have a great impact on thermohaline circulation, since they are the most significant source of salty water for the oceans all over the world (Carsey et al., 1991).

Finally, human activities can be affected by sea ice as well. Navigation is one of the most important issues on human activity. Oceanic transportation, fisheries and other marine activities at high latitudes may come across a trouble where first-year and multiyear ice covers. For example, Fig. 1.1 demonstrates a ship stuck in the ice. It can hardly move due to the thickness and strength of first-year or multiyear ice. In addition to the navigation concerns, marine creatures, marine operations (i.e. oil platform), and even human's traditional way of life (i.e. the fast ice edge is a productive hunting ground) (Casey, 2010) are likely to be impacted by sea ice.

Fig. 1.1 A ship stuck in Baltic Sea ice between Sweden and Finland's Aland Island (Jacobs, 2010)

In summary, sea ice plays critical roles in not only the Earth's climate system but also human activities, so detecting sea ice and obtaining a near-real time report are in demand.

1.2 Importance of SAR for Sea-Ice Detection

The first sea ice observation from coastal stations and ships may come back to more than 100 years ago, and use of satellite data has gradually been the most important observation method. Among different kinds of satellite data, Synthetic Aperture Radar (SAR) data is commonly considered outstanding. Satellite SAR data has the following three main advantages.

First, it permits wide area coverage like 50km-500km swath widths (Sandven and

Johannessen, 2006) and has relatively high spatial resolution from satellite altitudes, which is appropriate for sea-ice monitoring. For example, RADARSAT-2 with ScanSAR narrow beam mode has 300km swath widths and still keeps 50m spatial resolution (CSA, 2011), whereas, in spite of providing higher spatial resolution, optical instruments such as ASTER only cover 60km widths (SIC, 2012).

Second, utilization of microwave rays should be the most attractive point for satellite SAR, which can penetrate clouds, fog and other atmospheric substances, obtaining operational and reliable imagery. For example, in RADARSAT-2, C-band (8.0-4.0GHz, 3.8-7.5cm) (CSA, 2011) has relatively long wavelengths that can hardly be weaken by clouds and fogs, which are composed by small particles.

Third, especially for sea-ice detection, SAR is sensitive to ice type and surface roughness, meaning that it can provide us a lot of useful information content (Sandven and Johannessen, 2006). Moreover, polarization also provides different responses in terms of various ice types, resulting in some successful segmentation approaches based on fusion of different polarizations of SAR imagery (Li et al., 2009; Du et al., 2002).

SAR sea ice images acquired by Canada's RADARSAT-1 and -2 are increasingly received daily at the Canadian Ice Service (CIS) in Ottawa and are currently interpreted manually by well-trained human operators, which is time-consuming and inaccurate. As such, automatic detection of sea-ice coverage is urgently needed. Furthermore, as an indispensable part of automatic detection, automatic

segmentation has become the focus of this study.

1.3 Importance of Automatic Segmentation of SAR Sea-Ice Imagery

In image processing, segmentation and classification always play important roles. Image segmentation refers to clustering or grouping the homogeneous pixels into various groups while classification is next hierarchy which labels those clustered pixels as different classes. In this study, a primary task of sea-ice detection is to divide different ice types into segments, which contain different gray values, textures and other characteristics; and the classification depends on scientists' knowledge. Although easily segmented by human observer, there exists no robust automated approach that can consistently separate relevant categories in SAR sea-ice imagery (Jobanputra, 2004). Automatic approaches mainly have two advantages:

- They can liberate some human resources and save time. Although human cannot be replaced completely, applying a good automatic segmentation approach in a computer may be helpful in parallel processing large numbers of images, and assisting human's work via pre-processing.
- The results produced by a computer are consistent or unified, and often show more details. In fact, the same images operated by different people may lead to different results due to human's subjective reasons (i.e. carelessness). Conversely, given a confidence rate, a good automatic approach can guarantee a fair accuracy and provide segmentation results as detailed as possible.

There has been no perfect approach for SAR sea-ice segmentation so far. Considering the accuracy, stability and computational cost, existing approaches have more or less weakness or shortcomings. Therefore, alternative approach should be more accurate, more reliable, and most importantly, very fast. In this study, a new approach has been proposed in order to pursue these goals.

1.4 Objectives

The principal goal of this study is to propose a new alternative approach that can automatically segment SAR sea-ice imagery. In particular, this thesis focuses on the important role of suppressing speckle noise in SAR images and implements a new and effective filter to deal with it. In order to achieve these goals several sub-objectives have been set:

i. To identify how different ice types appear in SAR (in our case, RADARSAT-2) sea-ice images.

ii. To study the mechanism of formation of the speckle noise in SAR images and to develop a proper method in order to suppress the speckle noise.

iii. To find a proper algorithm so as to cluster the filtered images.

iv. To evaluate the effectiveness of our approach by using an appropriate and reliable method.

1.5 Structure of Thesis

The rest of the thesis is organized as follows. Chapter 2 provides a brief background on both the physical and electrometric properties of sea ice, the foundations of SAR, and the mechanism of speckle noise. Then several literature reviews of approaches of SAR sea ice segmentation are illustrated. In particular, some denoising methods for SAR imagery are discussed afterwards.

Chapter 3 mainly introduces the Conventional Bilateral Filter (CBF) and its modifications. Some discussion follows behind that.

In Chapter 4, the methodology of a two-phase approach is proposed for segmenting SAR sea-ice images, including first denoising image by Gamma-based Bilateral Filtering (GBF), and then clustering by K-means algorithm. Finally, an optional process is discussed.

Chapter 5 presents and discusses the experimental results obtained using both simulated and real SAR images.

Finally, Chapter 6 presents conclusions drawn from this study and recommendations for future work. It is clear that the proposed approach still has a large room to be developed.

Chapter 2

Background

2.1 Sea ice and SAR

In this study, the main goal is to segment SAR seaice imagery automatically. As the importance of that has been discussed in Chapter 1, knowing a clear definition of various ice types, the physical and electromagnetic properties of sea ice, the fundamentals of SAR, and the existing SAR sea-ice image segmentation approaches is necessary.

2.1.1 Ice Chart and Egg Code

One of the most interests on sea-ice monitoring should be segmenting different types of sea ice and seawater, which has been first standardized by the Sea Ice Working Group of the World Meteorological Organization (WMO). It employs the Ice Chart, which provides information about the type, concentration, and floe size of the ice components in the region. An example of daily ice chart that covers the sea area nearby the Island of Newfoundland in Canada is shown in Fig. 2.1. Sea ice in this map is divided into different segments, each of which is interpreted by an egg code (some numbers within an ellipse like an egg). In Fig. 2.1, the egg codes in red

rectangles demonstrate the condition of ice in our study area.

Fig. 2.2 presents the definition of egg code, which is used to indicate ice observations interpreted from radar imagery. The first row defines the total concentration of ice in the segment (Ct). The second row defines the partial concentration of each types of ice in the segment (Ca, Cb, Cc, Cd). The third row defines the stages of development of ice in the segment (So, Sa, Sb, Sc, Sd, Se). Finally the fourth row defines the forms of ice in the segment (Fa, Fb, Fc, Fd, Fe). In detail, Table 2.1 codes for sea-ice stages of development (from new ice to multiyear ice) based on the thickness of ice; and Table 2.2 shows the codes for various forms of ice based on the width of ice.

Notice that segments in ice chart usually cover relatively large-scale areas and egg code tends to show the overall concentrations of different types of ice in a single segment. In this situation, it is difficult for us to know how different types of ice are distributed in this relatively small segment. Therefore, segmentation approaches on small scale is in demand. Of course, ice chart and egg code can also play a critical role of providing some prior knowledge for the further segmentation and classification. According to the definition of egg code and the ice chart in Fig. 2.1, it is easy to see that there are new ice, gray or gray-white ice and first-year ice in our study area.

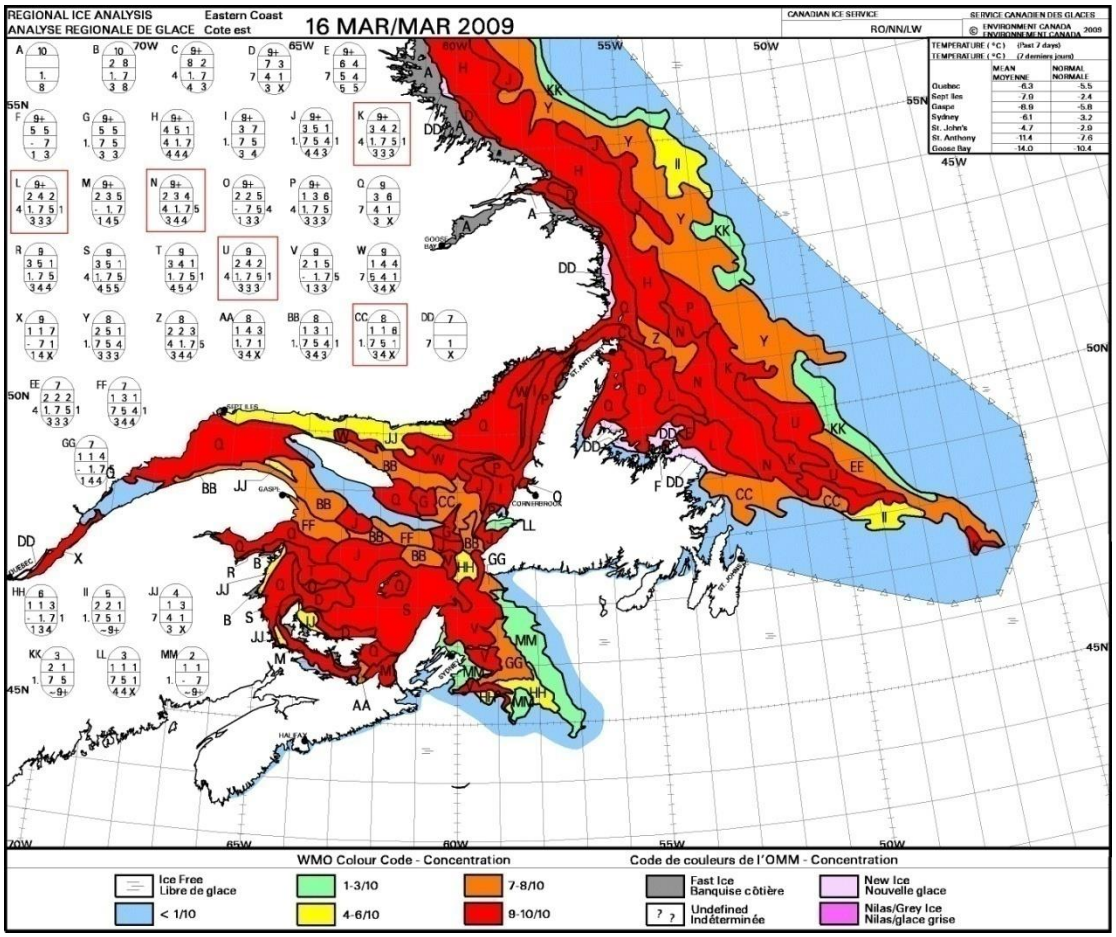

Fig. 2.1 Daily ice chart. The egg codes in red rectangular relate to the regions that cover our study area (CIS, 2009).

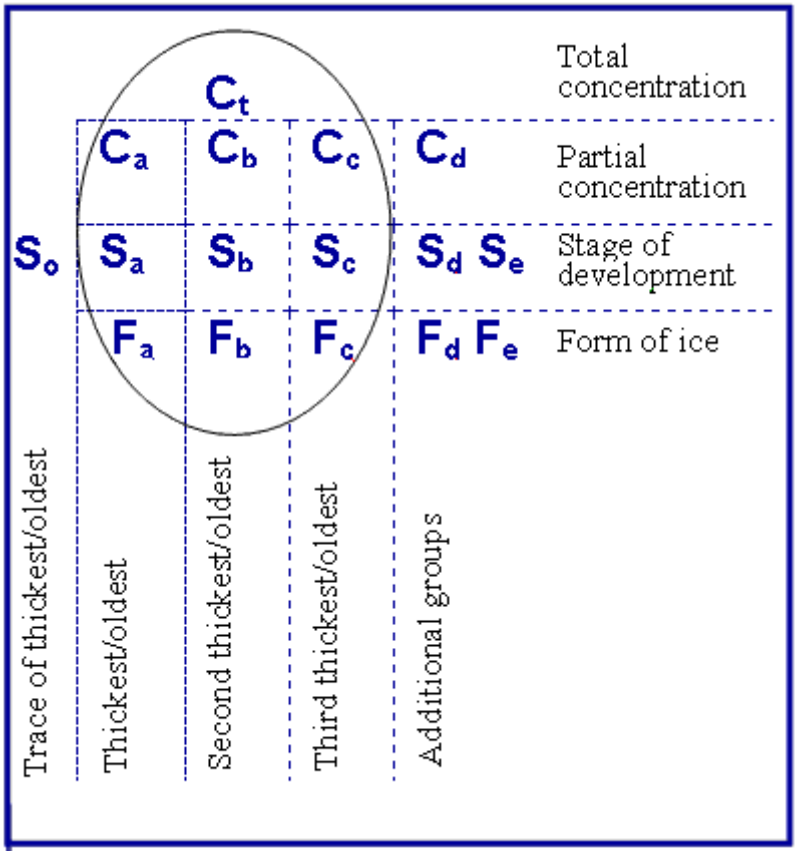

Fig. 2.2 Definition of the Egg Code (CIS, 2012).

Table 2.1 Coding for Sea-Ice Stages of Development (SoSaSbScSdSe) (CIS, 2012)

Description	Thickness (cm)	Code
New ice	< 10	1
Nilas, Ice rind	< 10	2
Young Ice	10 - 30	3
Gray Ice	10 - 15	4
Gray-white ice	15 - 30	5
First-year ice	>= 30	6
Thin first-year ice	30 - 70	7

First stage thin first-year	30 - 50	8
Second stage thin first-year	50 - 70	9
Medium first-year ice	70 - 120	1·
Thick first-year ice	> 120	4·
Old ice	-	7·
Second-year ice	-	8·
Multi-year ice	-	9·
Ice of land origin	-	▲.
Undetermined or unknown	-	X·

Table 2.2 Coding for Forms of Ice (FaFbFcFdFe) (CIS, 2012)

Description	**Width (m)**	**Code**
Pancake ice	-	0
Small ice cake, brash ice, agglomerated brash	< 2	1
Ice cake	2 - 20	2
Small floe	20 - 100	3
Medium floe	100 - 500	4
Big floe	500 - 2000	5
Vast floe	2000 - 10000	6
Giant floe	> 10000	7
Fast ice	-	8

Icebergs, growlers or floebergs	-	9
Undetermined, unknown or no form	-	X

2.1.2 Physical Properties of Sea Ice

In this section several physical properties of sea ice are introduced in order to make sense how they have impacts on the appearances of various ice types in satellite SAR imagery. WMO has a list of various types of sea ice shown in Table 2.3. In this study, it is necessary to understand the properties of new ice, gray ice and first-year ice, since these three types of ice cover the study area.

Table 2.3 Types of sea ice defined by the WMO (adapted from Casey, 2010)

Stage of Development (Ice Type)	**Definition**
New ice	A general term for recently formed ice. These types of ice are composed of ice crystals, which are only weakly frozen together (if at all) and have a definite form only while they are afloat. Here, new ice refers collectively to frazil, grease ice, nilas and pancake ice.
Frazil ice	Fine spicules or plates of ice, suspended in water
Grease ice	A later stage of freezing than frazil ice when the crystals have

	coagulated to form a soupy layer on the surface. Grease ice reflects little light giving the sea a matte appearance.
Nilas	A thin elastic crust of ice easily bending on waves and swell and under pressure, thrusting in a pattern of interlocking “fingers” (finger rafting). Has a matte surface and is up to 10 cm in thickness.
Pancake ice	Predominantly circular pieces of ice from 30 cm – 3 m in diameter, and up to about 10 cm in thickness, with raised rims due to the pieces striking against one another.
Young ice	Ice in the transition stage between nilas and First-year ice, 10-30 cm in thickness. May be subdivided into grey and grey-white ice.
Gray ice	Young ice 10-15 cm thick. Less elastic than nilas and breaks on swell. Usually rafts under pressure.
Gray-white ice	Young ice 15-30 cm thick. Under pressure more likely to ridge than to raft.
First-year ice	Sea ice of not more than one winter’s growth, developing from young ice; thickness 30 cm – 2 m. May be subdivided into thin First-year ice (30-70 cm thick), medium First-year ice (70-120 cm thick) and thick First-year ice (over 120 cm thick).

According to Sandven and Johannessen (2006), sea ice has several physical parameters, including temperature, salinity, crystal structure, surface roughness, snow, and water on the ice surface. The water on top of ice often occurs in summer when ice

and snow melt. As long as I consider, salinity, crystal structure, surface roughness and liquid water on top of the ice are more critical for radar remote sensing among these parameters of sea ice.

The formation of ice begins when the sea water reaches the freezing point. Then it is called frazil which is composed of small ice crystals. As freezing continues and more ice crystals are formed, the crystals coagulate to form grease ice in rough sea states or to form nilas under calm conditions (Casey, 2010). In general, sea ice with thickness of less than 10 cm is named as new ice. The new ice has considerable impact on SAR imagery of open sea water because either frazil ice or grease ice dampens the short gravity waves on the open sea water surface (Sandven and Johannessen, 2006). In this stage, the connection between ice crystals is so weak that pancake ice can be formed due to the effects of wind and waves. For SAR imagery in HH mode, new ice looks like open sea water because the small thickness results in most incoming radiation passing through the ice into the sea water. For example, in Fig. 2.3, the new ice (actually nilas, marked by triangle) is darkest and has little speckle, which is similar to sea water as water can absorb most incoming radiation.

As the new ice grows thicker and becomes less elastic, it forms gray ice (10–15 cm), gray-white ice (15–30 cm) and eventually first-year ice (>= 30 cm). During this stage, congelation growth (water molecules freezing to ice crystals at the ice-seawater interface) becomes dominant (Casey, 2010). In detail, as the ice crystals enfolds and

compress the brine, the voids of air among brine pockets are replaced by brine drainage, leading to the visual appearance from almost black new ice to bright gray ice, and eventually much bright first-year ice in SAR images (Sandven and Johannessen, 2006). The rectangles in Fig. 2.3 represent the gray ice which looks brighter than new ice and has much more speckles. Of course, as congelation growth continues, the gray ice get thicker and brighter visually. When the thickness reaches 30 cm, it turns to the first-year ice (shown in Fig. 2.3, marked by circles).

Salt is released after ice is formed from the water and continuously runs off in the upper layer over time (Sandven and Johannessen, 2006), so the newer the ice is, the higher salinity it has. With changes of salinity the crystal structure also changes, which makes the most contribution to different appearances in SAR imagery in terms of new ice, gray ice and first-year ice. In addition, since the freezing point of ice is below zero degree, increasing surface temperature may cause ice or snow melting and forming water ponds on top of the ice. In general, these water ponds can show the dark spots in SAR images for the first-year sea ice (Casey, 2010). Finally, surface roughness is mainly determined by weather conditions (new ice and young ice) and deformation (first-year ice). Surface roughness of new ice is easy to be affected by wind and waves. For example, if the nilas is broken by waves, after it freezes again, pancake ice may form, which completely differs from the nilas (Casey, 2010). However, this change is meaningless for SAR monitoring because sea water is dominant in this stage. On contrary, for the first-year ice, deformation occurs “when

ice is subject to compacting ice motion (due to convergent ice drift) the stress (Casey, 2010, pp. 14)". The deformed ice can be further divided into ridging and rafting. The ridging, rafting or other processes can generate various roughnesses of surface, which are much properly observed by SAR, because radar backscatter shows significant contrast between rough and smooth ice surfaces (Sandven and Johannessen, 2006).

In summary, the physical properties of sea ice are not determined by a single factor. In my opinion, salinity, temperature and crystal structure play the most primary roles in not only the formation of sea ice but also the appearance in SAR imagery.

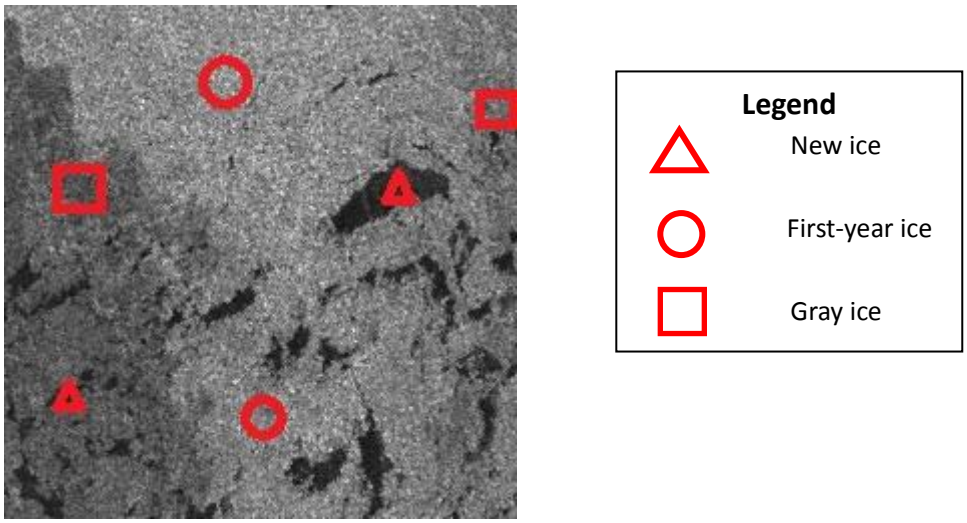

Fig. 2.3 Different types of sea ice in SAR imagery

2.1.3 Electromagnetic Properties of Sea Ice

Electromagnetic properties of sea ice are critical for microwave remote sensing as well. To make a better interpretation of backscatter from sea ice, one should understand the electromagnetic properties of each component of sea. Of course, characteristics of SAR should also be considered due to their effects on electromagnetic properties of sea ice.

Two fundamental electromagnetic properties of surface are *reflection* and *emission* (Sandven and Johannessen, 2006). The latter can be governed by a dimensionless coefficient called emissivity, which can be calculated by the complex dielectric constant (or the relative permittivity) expressed by

$$\varepsilon = \varepsilon' + j\varepsilon'' \tag{2.1}$$

where ε' is the dielectric constant, ε'' is the dielectric loss factor and $j = \sqrt{-1}$ (Sandven and Johannessen, 2006; Hallikainen and Winebrenner, 1992). In addition to *emission*, *reflection* can be determined by reflection coefficient r which is defined as:

$$r = \left|\frac{n-1}{n+1}\right|^2 \tag{2.2}$$

where $n^2 = \varepsilon$ denotes complex index of refraction (Sandven and Johannessen, 2006).

Since reflection coefficient r can be calculated from complex dielectric constant ε, emissivity can just be regarded as the representation of electromagnetic properties. In general, higher emissivity means more backscatter, which is determined by the dielectric constant and surface roughness of objects (Sandven and Johannessen, 2006).

For saline ice, the dielectric constant is high and "strongly dependent on both temperature and salinity of ice" (Sandven and Johannessen, 2006, pp. 13). In detail, the dielectric constant decreases as the temperature decreases (Sandven and Johannessen, 2006) because temperature controls the brine volume in ice as the dielectric constant is strongly dependent on brine volume (Casey, 2010). Meanwhile brine itself, of course, also has a great influence on the dielectric constant of ice due to its high dielectric loss factor that causes attenuation when incident microwave radiation goes through the ice layer. As a result, saline ice types produce less backscatter whereas less saline ice types produce more backscatter (Casey, 2010).

Roughness on top of ice plays a critical role for emissivity as well. When wavelength of incident radiation is nearly as same as the size of objects, a defuse scattering will occur, leading to high emissivity. On contrary, if wavelength of incident radiation is large enough, reflection will play a dominant role. Therefore, the frequencies of remotely sensed instruments have a significant impact on how surface roughness

affects emissivity or backscatter (Casey, 2010).

2.1.4 Fundamental Parameters of SAR

The imaging geometry of present spaceborne SAR systems is shown in Fig. 2.4. More details of SAR systems can be found in Sandven and Johannessen (2006). There are many factors that can influence backscatter: wavelength of incident signal, incident angle, number of looks and polarization. For sea-ice monitoring, X-band (12.5-8.0 GHz, 2.4-3.8cm) or C-band (8.0-4.0 GHz, 3.8-7.5cm) are more appropriate, since shorter wavelength (i.e. K-band (30 GHz, 1cm)) may cause radiation significantly attenuated by the atmosphere and longer wavelength (i.e. L-band (2.0-1.0 GHz, 15-30cm)) has too coarse spatial resolution (Clausi, 1996).

Radar remote sensing is more sensitive to the surface roughness compared with visual or infrared remote sensing (Sandven and Johannessen, 2006). If the surface is smooth, specular reflection occurs on the surface and little radiation can be received by sensors for off-nadir viewing. On the other hand, if the surface becomes rougher, more diffuse reflection will occur. Hence roughness on the surface is able to control the amount of backscatter that can be received by sensors. For SAR system, whether the surface is considered rough or not can be judged by the Rayleigh criterion:

$$h < \frac{\lambda}{8\cos\theta} \tag{2.3}$$

where h is the root mean square (rms) height of the surface, θ is the incident angle and λ is the signal wavelength (Clausi, 1996). The surface is considered smooth if the Rayleigh criterion is true while rough if the Rayleigh criterion is false. It is obvious that angle of incidence deeply affects the behavior of backscatter as the range distance increases. However, for the spaceborne SAR this problem can be ignored because high flight path of satellites let the angle of incidence almost holds a constant over the same effective area (Clausi, 1996).

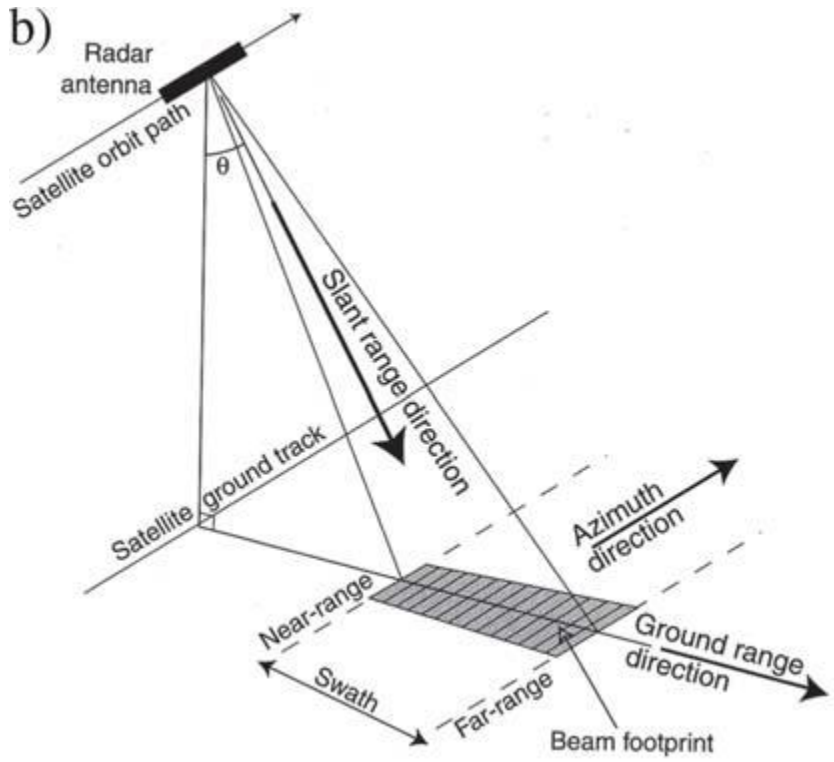

Fig. 2.4 The imaging geometry of present spaceborne SAR systems (adapted from Sandven and Johannessen, 2006)

Speckle is always an important point for SAR imagery. “Speckle arises from the coherent nature of radar waves, causing random constructive and destructive

interference and, hence, random bright and dark areas in radar imagery" (Lillesand and Kiefer, 1987, pp. 499). A typical two-class example of SAR image is illustrated in Fig. 2.5. It is easily observed that significant amount of speckle degrades the image since its histogram (shown in Fig. 2.6) forms nearly a unimodal shape, meaning that it is difficult for computer to distinguish the two classes. Multiple looking processing has ability of reducing the amount of speckle via averaging images of the same region and how many images are used to be averaged is recorded as the number of looks (Clausi, 1996). It is a basic parameter usually provided by the producer. The amount of speckle has an inverse relationship with the number of looks while the resolution cell size has a direct relationship with the number of looks (Lillesand and Kiefer, 1987).

Polarization is also an important parameter for SAR system. There are two kinds of manners to transmit or receive signals: horizontal (H) and vertical (V); thus, four modes can be created: HH, VV, HV and VH. Different polarization modes can lead to different types of backscatter returns, then different SAR images (Clausi, 1996).

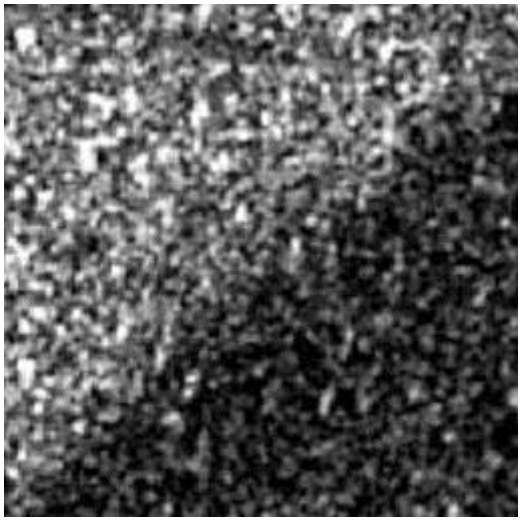

Fig. 2.5 Typical two-class SAR image with speckle (adapted from Kwon et al., 2012)

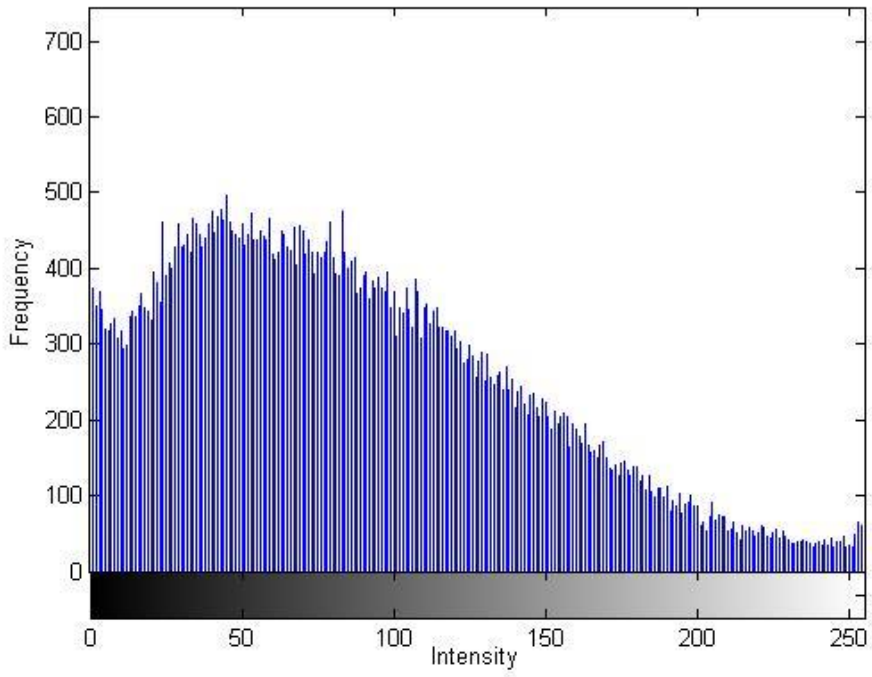

Fig. 2.6 The histogram of SAR image in Fig. 2.5

2.2 SAR Sea-Ice Image Segmentation

There are many studies on SAR image segmentation but relatively less concentrating

on SAR sea-ice imagery. Typically, these approaches can be divided into three categories: pixel-based approaches, texture-based approaches and other approaches (Wackerman et al., 1988).

Indeed, "Other approaches" mentioned above are some sort of supervised methods like Artificial Neural Network (ANN) and Expert System (ES). Karvonen (2004) proposed a method for SAR sea-ice segmentation and classification using modified pulse-coupled neural networks, and Soh et al. (2004) provided an ES named ARKTOS for the same task. These supervised methods always require *a priori* knowledge to train the data so as to build up their models or rules for segmenting images. However, little researches about this can be seen in recent years because supervised methods are not appropriate in practice due to more human involvement and low automation. Therefore, more attention will be paid to the pixel-based approaches and texture-based approaches in following content.

2.2.1 Texture-based Approaches

Texture-based approaches are popular for SAR sea-ice segmentation recently, since distinct textural patterns of different types of ice, especially the pancake ice which has strong texture, can be illustrated by SAR imagery. They often first extract features by taking in to account the correlation of pixels (not just single pixel's intensity), then reduce the amount of features in order to select optimal ones, and finally segment by

some grouping methods such as edge detection (Jobanputra and Clausi, 2006) or K-means iterative Fisher (KIF) algorithm (Clausi, 1996).

Gray level co-occurrence is one of the most widely used texture features. Based on gray level co-occurrence matrix (GLCM) (Soh et al., 1999) and gray level co-occurrence probability (GLCP) (Jobanputra and Clausi, 2006), one can effectively reduce the effect of noise and improve the accuracy of segmentation. Markov Random Field (MRF) is another important texture-based algorithm. There is a large amount of literature on image segmentation using MRF (Descombes et al., 1996; Weisenseela et al., 1999; Deng and Clausi, 2005; Benboudjema et al., 2007; Yang and Clausi, 2009;). MRF can be combined with model-based segmentation or clustering to take into account the spatial relationship between pixels (Wang, 2006). It is assumed that the class probability of a pixel is only dependent on class relationships of its (spatial) neighbor clusters, so that it reduces the possible influence and overlapping clusters (Tran et al., 2005).

However, texture-based approaches have their weakness that pixels located near the texture boundaries are likely to be misclassified (Kwon et al., 2012). More importantly, some of these approaches have low computational efficiency (i.e. generating a GLCM of 256 x 256 SAR image with 6 features takes more than one minute under Intel(R) Core(TM)2 2.13 GHz CUP according to my experience), which is not suitable for operational applications. Finally, in this study, there is no strong

texture features (i.e. In Fig. 2.3, it is hardly observed strong texture in homogenous areas due to the calm ocean states.), so texture analysis cannot make a difference in this study.

2.2.2 Pixel-based Approaches

The pixel-based approaches are based on the behavior of the intensity of the individual pixels. They usually have an assumption that pixel intensities are identically distributed and independent (Wackerman et al., 1988).

Global thresholding (Otsu, 1979) is the simplest and earliest SAR segmentation methods based on pixels. Then it was developed to adaptive thresholding methods soon. For example, the dynamic thresholding algorithm proposed by Haverkamp et al. (1993) first chooses thresholding values from local regions and then thresholds the entire image. As it accounts for the local variance in an image, it meets success in segmenting the sea ice images which have an obviously bimodal gray-level distribution. Moreover, the finite Gamma mixture model was originally applied by Samadani (1995) to estimate proportions of ice types in a SAR image. The method uses a mixture model based on assuming a Gamma distribution for each of the ice classes and uses an iterative method to estimate the parameters of the distribution function. Another one that should be mentioned is the K-means clustering method first proposed by Hartigan et al. (1979), which is applied as a step in this approach

and as a comparison as well. It can be used to cluster feature vectors and generate image segmentations. All of these three methods have a basic assumption of intensity distribution, so their performances significantly depend on how accurately the intensity distribution is modeled. In addition, since they are all global methods that do not consider the spatial relationship of the image pixels, they are inevitably sensitive to image noise. Hence a filter must be first employed in order to reduce the influence of speckle noise.

2.2.3 Summary of Segmentation Approaches

Table 2.4 summarizes the advantages and disadvantages of different kinds of segmentation methods.

Table 2.4 Advantages and disadvantages of categories of segmentation methods

Categories of segmentation methods	**Typical techniques**	**Advantages**	**Disadvantages**
Pixel-based	Thresholding; adaptive thresholding; K-means algorithm;	• Low complexity; • High computational efficiency; • Stable;	• Sensitive to noise; • Low accuracy;

Texture-based	Gray level co-occurrence matrix; Markov random field; Fourier transform; Semivariance;	• High accuracy; • Good at locating directional features such as ridge lines; • More information about the image; • Flexibility;	• Long computing time; • Unreliable boundaries;
Others	Artificial neural network; expert system	• Flexible; • Adaptive;	• Using a prior data; • Hard to know the details about the classifier;

2.3 Filtering Techniques

In order to reduce the image noise, filtering is usually applied as pre-processing. As more and more new and powerful filtering techniques have been carried out, the importance of filtering increases rapidly. Particularly for SAR imagery, which carries quite a lot speckle noise, a filtering phase may be indispensable.

In the case of SAR image segmentation, the most commonly used domain filters can be Lee filter (Lee, 1980), Kuan filter (Kuan et al., 1987), Frost filter (Frost et al., 1982), Gamma Filter (Lopes et al., 1993), and Anisotropic Diffusion (Yu and Action,

2002). (Strictly speaking, Anisotropic Diffusion is not a filter. However, since it also aims to reduce the image noise, it could be discussed with other filters together in this section.) All these filters have an adaptive scheme in order to smooth image in homogeneous areas while preserving edges. For further understanding the filters, their brief equations will be illustrated in the following context.

A. Lee Filter and Kuan Filter

Both the Lee filter and the Kuan filter are based on the Minimum Mean Square Error (MMSE) criterion. Indeed, the Lee filter is a particular case of the Kuan filter (Gagnon and Jouan, 1997). A linear speckle model can be written in the following form as a weighted sum of the observed and mean values:

$$\widehat{R}(t) = \bar{I}(t) + W(t)\big(I(t) - \bar{I}(t)\big) \tag{2.4}$$

where $\bar{I}(t)$ is the mean value of the intensity within the filter window S, and $W(t)$ is the weighting function.

For the Kuan filter, W(t) is given by:

$$W(t) = \frac{1 - \frac{C_u^2}{C_I^2(t)}}{1 + C_u^2} \tag{2.5}$$

where

$$C_I^2(t) = \frac{1}{N}\frac{\sum_{t\in S}(I(t) - \bar{I}(t))^2}{(I(t) - \bar{I}(t))^2} \tag{2.6}$$

and Cu is the noise variation coefficient determined by:

$$C_u = \frac{\sigma_u}{\bar{u}} \tag{2.7}$$

For the Lee filter, Eq. (2.5) can be modified as:

$$W(t) = 1 - \frac{C_u^2}{C_I^2(t)} \tag{2.8}$$

From above equations it is evident that coefficient of variation Cu is critical because the ability of smoothing in homogenous areas while preserving edges depends on this statistics in the window. When $C_I(t)$ approaches C_u, then W(t) approaches to 0, the filter behaves like a mean filter; when $C_I(t)$ approaches ∞, then W(t) approaches to 1, the filter does nothing on the image.

B. Frost Filter

The Frost filter is a sort of the Wiener filter. It can adaptively convolve the pixel values within a fixed window (Gagnon and Jouan, 1997). The filter output is determined by:

$$\widehat{\mathrm{R}}(\mathrm{t}) = \sum_{\mathrm{t}\in\mathrm{S}} \mathrm{mI}(\mathrm{t}) \tag{2.9}$$

where the exponential impulse response m is given by Yu and Action (2002):

$$\mathrm{m}(\mathrm{t}) = \mathrm{K}_1 \exp(-KC_u(t_0)|t|) \tag{2.10}$$

where K is the damping factor, t_0 represents the location of current pixel, |t| is the distance measured from t_0, $\mathrm{C_u} = \frac{\sigma_\mathrm{u}}{\bar{\mathrm{u}}}$ is the observed coefficient of variation, and K_1 normalizing constant. When $\mathrm{KC_u}(\mathrm{t}_0)$ approaches to 0, then the filter behaves like a mean filter; conversely, at an edge $\mathrm{KC_u}(\mathrm{t}_0)$ becomes so large that the filtering is inhibited completely.

Since above three filters are based on a linear model, their ability of preserving edges significantly depends on the window size. A too large window size (compared to the scale of interest) will cause over-smoothing and blur edges. However, a small window size can lead to impairing the power of smoothing in homogenous areas and leaving the noise (Yu and Action, 2002). As a consequence, extent versions of the Lee filter and the Frost filter have been introduced to alter performance locally according to three cases (Lopes et al., 1990, 1993). In the first case, the local coefficient of variation is below a lower threshold, so averaging is applied. Additionally, when it is above a higher threshold, the filter acts as an all-pass (identity) filter. Finally if it locates between the two thresholds, a balance should be made between the mean and

identity filters (Yu and Action, 2002).

C. Gamma Filter

The Gamma filter is a maximum a posteriori (MAP) based on Bayesian analysis of the images statistics (Lopes et al., 1993). It assumes that the reflectivity and speckle are both the Gamma-distributed, and then the observed intensity is K-distributed (Gagnon and Jouan, 1997). The Gamma-Gamma MAP estimate is given by:

$$\widehat{R} = \frac{(\alpha - L - 1)\langle R\rangle + \sqrt{\langle R\rangle^2(\alpha - L - 1)^2 + 4\alpha L I\langle R\rangle}}{2\alpha} \tag{2.11}$$

where

$$\alpha = \frac{L + 1}{L(\frac{\sigma_I}{\langle R\rangle})^2 - 1} \tag{2.12}$$

where L is the number of looks, I is the observed intensity, $\langle R\rangle$ is a *priori* mean (Lopes et al., 1993).

Unlike the Lee and Kuan filters, $\widehat{R}$ is a nonlinear function of I and $\langle R\rangle$. Under homogenous conditions, α tends towards infinity, then $\widehat{R}$ becomes the same as $\langle R\rangle$. On the other hand, when L tends towards infinity, the MAP estimate is observed intensity I itself, which is expected as there is no more speckle noise (Lopes et at., 1993).

D. Anisotropic Diffusion

Anisotropic Diffusion initially based on the nonlinear partial differential equation (PDE) for smoothing images in homogenous areas (Yu and Action, 2002):

$$\begin{cases} \frac{\partial I}{\partial t} = \mathrm{div}[c(|\nabla I|) \cdot \nabla I] \\ I(t=0) = I_0 \end{cases} \tag{2.13}$$

where ∇ is the gradient operator, div is the divergence operator, $c(|\nabla I|)$ is the diffusion coefficient, and I_0 is the original image. Perona and Malik (1990) suggested two functions for diffusion coefficient:

$$c(|\nabla I|) = e^{-(\frac{|\nabla I|}{k})^2} \tag{2.14}$$

and

$$c(|\nabla I|) = \frac{1}{1 + (\frac{|\nabla I|}{k})^2} \tag{2.15}$$

where k controls the sensitivity to edges and is usually chosen experimentally or as a function of the noise in the image.

When $|\nabla I| >> k$, then $c(|\nabla I|)$ tends to 0, and it acts as an all-pass filter; when

$|\nabla I| << k$, then $c(|\nabla I|)$ tends to 1, and it becomes a Gaussian filter (Yu and Action, 1993). The resulting image is a combination between original image and a filter that depends on local content of original image. As a result, anisotropic diffusion is a nonlinear method. However, anisotropic diffusion still has drawback that the convergence of the diffusion process is time-consuming. In addition, as an iterative algorithm, the selection of parameters such as the scaling factor and the time step can be difficult, resulting from a balance has to be made between algorithm's performance and time-consuming.

In general, even though typical filters have been commonly used for SAR imagery, their limitation directs us to introduce a new filter: Bilateral Filter. This nonlinear and non-iterative filter is widely used in computer vision field, for example, achieves a success in medical imagery processing, which is likely to be attractive for SAR image processing as well. In this project, actually the most important contribution is to adopt and modified the Bilateral Filter, then achieving a better performance in the filtering or denoising phase.

Chapter 3

Bilateral Filtering

3.1 Conventional Bilateral Filter

Consider the input data denoted as f can be represented as multiplication of real gray value g and noise n:

$$f = g * n \tag{3.1}$$

The aim for filtering or denoising is to suppress noise n in order to extract g from f. In spatial filtering, the output data g is usually obtained by using a local filter:

$$g(x) = k^{-1}(x) \int_{-\infty}^{\infty} \int_{-\infty}^{\infty} f(\xi) c(\xi, x) d\xi \tag{3,2}$$

where x represents current pixel, ξ represents neighbor pixel from x, $c(\xi, x)$ represents the *spatial closeness* between ξ and x, and k(x) is the normalization:

$$k(x) = \int_{-\infty}^{\infty} \int_{-\infty}^{\infty} c(\xi, x) d\xi \tag{3.3}$$

In the case of Gaussian filtering, the spatial closeness can be expressed by:

$$c(\xi, x) = e^{-\frac{1}{2}(\frac{\|\xi - x\|}{\sigma})^2} \tag{3.4}$$

where the $\|\xi - x\|$ is the Euclidean distance between x and ξ, σ is standard deviation.

The Gaussian low-pass filter has a strong ability to smooth the image. However, it will greatly blur the boundaries when used for filtering. Therefore, Tomasi and Manduchi (1998) first came up with a filter named Bilateral Filter (BF) based on human perception through incorporating the *similarity of intensity* (or range), and others gradually improve its mathematical theory (Pianykh, 2010; Elad, 2002).

In Conventional Bilateral Filtering (CBF), given a window, the centre pixel x's value can be estimated by the weighted average of nearby pixels ξ. According to Tomasi

and Manduchi (1998), given the input image f(x), the output image g(x) can be expressed by:

$$g(x) = k^{-1}(x) \int_{-\infty}^{\infty} \int_{-\infty}^{\infty} f(\xi) c(\xi, x) s\big(f(x), f(\xi)\big) d\xi \tag{3.5}$$

where k(x) is normalization:

$$k(x) = \int_{-\infty}^{\infty} \int_{-\infty}^{\infty} c(\xi, x) s\big(f(x), f(\xi)\big) d\xi \tag{3.6}$$

.

The local filter of CBF is a combination of two terms (filters): spatial filter $c(\xi, x)$ and range filter $s\big(f(x), f(\xi)\big)$. The spatial filter $c(\xi, x)$ describes the spatial closeness while the range filter $s\big(f(x), f(\xi)\big)$ describes the similarity of intensity (or range) between ξ and x. In the Gaussian case, the spatial filter is defined as follows:

$$c(\xi, x) = e^{-\frac{1}{2}\left(\frac{\|\xi - x\|}{\sigma_d}\right)^2} \tag{3.7}$$

where $\|\xi - x\|$ is the Euclidean distance between x and ξ, and σ_d is the spatial spread in the domain. The range filter can be expressed by:

$$s\big(f(x), f(\xi)\big) = e^{-\frac{1}{2}\left(\frac{|f(\xi) - f(x)|}{\sigma_r}\right)^2} \tag{3.8}$$

where $|f(\xi) - f(x)|$ is the absolute difference of pixel intensities between ξ and x,

and σ_r is the photometric spread in the image range.

On the one hand, if two pixels are nearer, their gray values should be more similar. Based on this assumption, a Gaussian filter has the ability of smoothing images. It can be effective in homogenous areas but may fail in the areas that contain edges and strong textures; because it will blur the edges and textures that should be kept. Therefore, a range filter is incorporated to preserve them. On the other hand, according to Tomasi and Manduchi (1998), the spatial distribution of image intensities plays no role in range filter taken by itself, meaning that if the range filter is applied alone, results can be as the same as the original images. But when combining it to the previous spatial filter, something interesting occurs, that is, the CBF has significant effect on smoothing while preserving the edges. The effectiveness of this combination is shown in Fig. 3.1.

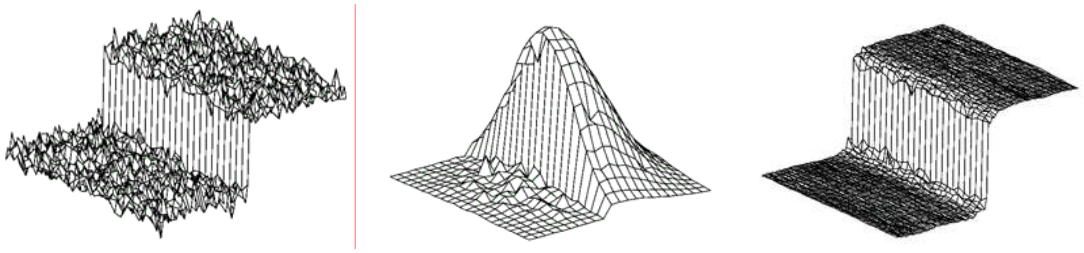

(a) (b) (c)

Fig. 3.1 (a) A 100-gray-level step perturbed by Gaussian noise with σ_d=10 gray levels; (b) Combined similarity weights $c(\xi,x)s\big(f(x),f(\xi)\big)$ for a 23x23 neighborhood centered two pixels to the right of the step in (a); (c) The step in (a) after bilateral filtering with σ_r=50 gray levels and σ_d=5 pixels. (adapted from

Tomasi and Manduchi, 1998)

3.2 Sensitive Analysis

For a sensitive analysis of CBF, Equivalent Number of Looks (ENL) is used to test the smoothing capacity in homogeneous regions because the larger ENL indicates the smoother results (Anfinsen et al., 2008). The ENL is given by Walessa and Datcu (2000):

$$\mathrm{ENL} = \frac{\mathrm{E}^2(\mathrm{I})}{\mathrm{Var}(\mathrm{I})} \tag{3.9}$$

where E(I) and Var(I) are the expectation and variance for the image I, respectively. In addition, the Edge Preserve Index (EPI) (Zhang et al., 2009) is adopted to evaluate the effectiveness of preserving details in heterogeneous regions as follows:

$$\mathrm{EPI} = \frac{\sum \sqrt{[\mathrm{p_f}(\mathrm{i},\mathrm{j}) - \mathrm{p_f}(\mathrm{i}+1,\mathrm{j})]^2 + [\mathrm{p_f}(\mathrm{i},\mathrm{j}) - \mathrm{p_f}(\mathrm{i},\mathrm{j}+1)]^2}}{\sum \sqrt{[\mathrm{p_o}(\mathrm{i},\mathrm{j}) - \mathrm{p_o}(\mathrm{i}+1,\mathrm{j})]^2 + [\mathrm{p_o}(\mathrm{i},\mathrm{j}) - \mathrm{p_o}(\mathrm{i},\mathrm{j}+1)]^2}} \tag{3.10}$$

where $\mathrm{p_f}(\mathrm{i},\mathrm{j})$ represents the filtered image at position (i, j), $\mathrm{p_o}(\mathrm{i},\mathrm{j})$ represents the original image at position (i, j). Note that the EPI of original image is one, and the larger EPI means stronger power to preserve the edges.

According to Zhang et al. (2009), given σ_d=3, the relationship of normalized ENL and EPI versus σ_r is shown in Fig. 3.2; given σ_r=0.12, the relationship of normalized ENL and EPI versus σ_d is shown in Fig. 3.3. Zhang et al. (2009) suggest that the parameters corresponding to the crossing points in Figs. 3.2 and 3.3 should be the optimal choice. However, visually evaluation indicates that cannot achieve the best results because for SAR data, the "balance" of ENL and EPI does not mean the best. Fortunately, this method provides a way to analyze the sensitivity of parameters for BF. According to the Figs. 3.2 and 3.3, it is obvious that as σ_d and σ_r increase, their influence to the results weaken rapidly.

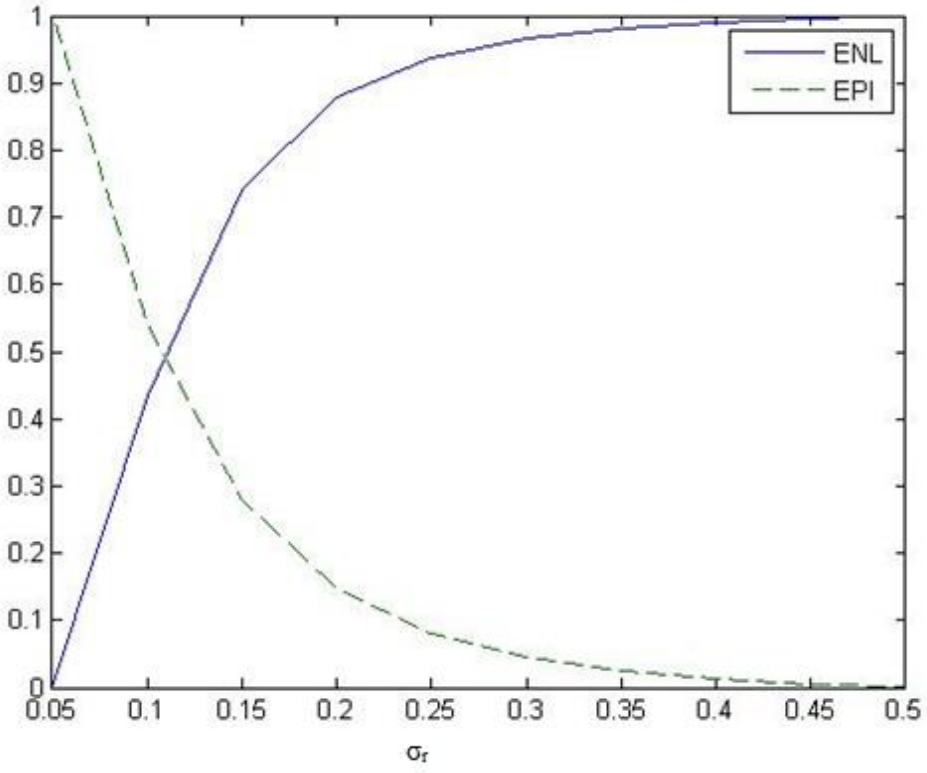

Fig. 3.2 ENL and EPI versus σ_r (σ_d=3)

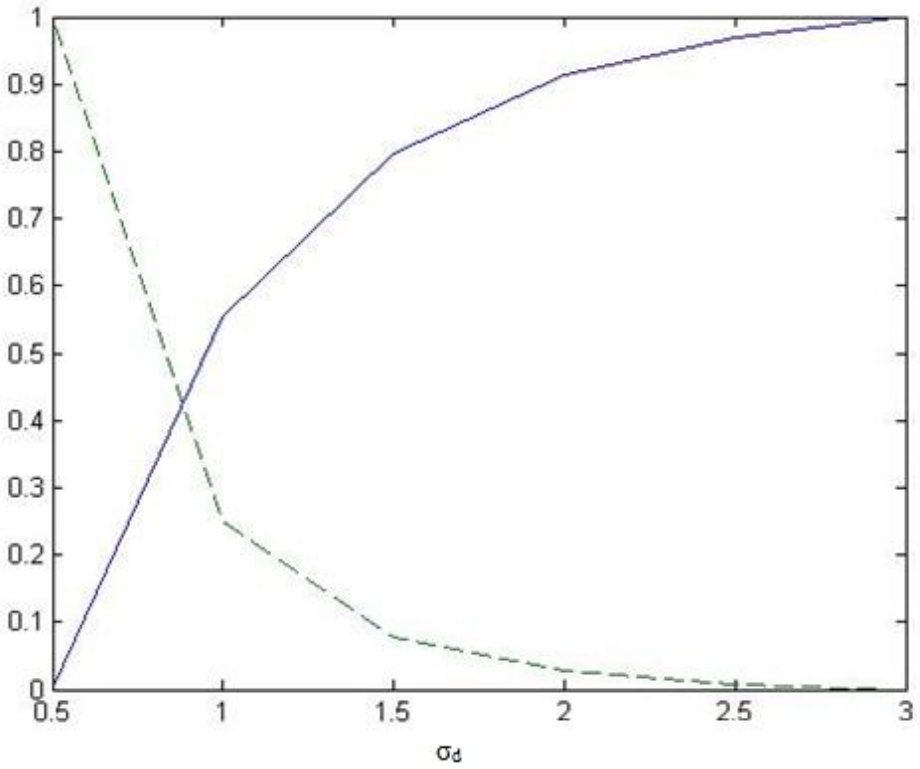

Fig. 3.3 ENL and EPI versus σ_d (σ_r=0.12)

3.3 Advantages of CBF

The most important advantage of CBF is its ability to smooth images while preserving edges by means of nonlinear combination of nearby image values. In other words, the CBF replaces each pixel by a weighted average of its neighbors. The weight assigned to each neighbor determines its influence on the result and is crucial to the output quality (Paris et al., 2009). In addition to the most critical advantage, other advantages can be listed as follows (Paris et al., 2009):

- Its simple formulation: this is of importance because the low complexity

makes it easy to understand, implement and then improve it.

- Only two parameters have to be determined in terms of the size and range difference of observations.
- It is a non-iterative approach. Thus the computational time is efficient and the parameters are easy to be set becaue their effect is not cumulative over several iterations.
- Based on efficient numerical schemes (Chaudhury et al., 2011; Elad, 2002; Weiss, 2006; Durand and Dorsey, 2002), its time cost can become lower.

Last but not least, the CBF is a robust filter as well. Durand and Dorsey (2002) studied the bilateral filter according to the framework of robust statistics. They indicated that as a robust term, the range filter can distinguish the *inliers* and *outliers*. In fact, the bilateral filter follows this strategy: there are little relationships and interactions between pixels that have different intensities; conversely, pixels with similar intensities should be greatly related and impact each other. This strategy is mainly defined or described by range weight (Paris et al., 2009).

Although there are several advantages of CBF, it cannot become a general approach for every application, especially for SAR imagery. Therefore, researchers have been continuously improving the CBF according to the actual situations.

3.4 Modifications of Bilateral Filter

Since CBF was proposed by Tomasi and Manduchi (1998), many researchers began to make a development in it. Except the methods that purely accelerate the computational efficiency (Chaudhury et al., 2011; Weiss, 2006; Durand and Dorsey, 2002), the main attention is paid to the methods that can improve the performance of CBF in this section. Although some of these approaches have not been used for SAR imagery, their algorithm is worth learning and consulting as well.

The simplest way to use BF is to combine it to other algorithms. Yang and Clausi (2007) proposed an approach for SAR sea ice segmentation based on edge-preserving watershed. In fact, the "edge-preserving" ability comes from the BF that is applied as a pre-processing before watershed algorithm. Moreover, Zhang and Gunturk (2008) presented a multi-resolution bilateral filtering for image denoising. They combine BF and wavelet decomposition as a new framework, and indicate that BF can eliminate low-frequency noise components. However, even though the BF is used in their approaches, there is no "real" improvement of BF because the BF itself is not improved or modified.

In bilateral filtering, there are two parameters, spatial spread σ_d and photometric spread σ_r, which are difficult to be determined. Someone sets them by empirical *trial and error* (Tomasi and Manduchi, 1998) while others try to make them adjusted by

some criterions.

Wong (2008) modified CBF using local phase characters. Based on the human perception system, the maximum moment of phase coherence is computed and added to BF in order to adjust BF's parameters. This algorithm has a good performance where noise level is high. Zhang et al. (2009) determine the parameters of BF via the evaluation indexes, including the equivalent number of looks (ENL) and the edge save index (ESI). In detail, they make one of the parameters constant and another changeable, apply the BF using these parameters, and then calculate the ENL and ESI. Since ENL and ESI have inverse relationship, the optimal parameters can be determined by drawing their curves and picking up the parameters in terms of the point of intersection. However, there is a conflict between computing time and accuracy of parameters' estimation. As the amount of pairs of parameters increases, the computing time increases rapidly whereas the accuracy of parameters' estimation raises little.

In addition to adjusting the two parameters adaptively, the formulation of BF can also be modified. Zhang and Allebach (2007) add an offset in the range filter. The modified range filter is defined as:

$$s\big(f(x), f(\xi)\big) = e^{-\frac{1}{2}\left(\frac{f(\xi)-f(x)-\zeta(x)}{\sigma_r(x)}\right)^2} \tag{3.11}$$

where the $\zeta(x)$ is an offset. In the sliding window S, let MIN, MAX, and MEAN denote the operations of taking the minimum, maximum, and average value of the data in S. The offset $\zeta(x)$ can be expressed by:

$$\zeta(x) = \begin{cases} MAX(S) - f(x), & \text{if } \Delta > 0 \\ MIN(S) - f(x), & \text{if } \Delta < 0 \\ 0 \quad\quad\quad\quad\quad\quad , & \text{if } \Delta = 0 \end{cases} \tag{3.12}$$

here,

$$\Delta = f(x) - MEAN(S) \tag{3.13}$$

This mean-shift operation can significantly sharpen the image at edges. However, the authors point out that shifting the range filter based on Δ is very sensitive to noise. Hence it may not obtain good results for dealing with SAR imagery where high-level speckle noise exists.

Another enhanced BF was proposed by Huang and Fuh (2006). They used other equations to replace Gaussian function in both spatial and range filter. The spatial filter is defined as following:

$$c(\xi, x) = \frac{1}{\|\xi - x\|^2 + 1} \tag{3.14}$$

where $\|\xi - x\|$ is the Euclidean distance between x and ξ. And the range filter is

replaced by a hybrid function which combines the alpha-trimmed filter and the single difference function:

$$s\big(f(x), f(\xi)\big) = \frac{1}{\left\lfloor \frac{|f(\xi) - f(x)|}{\sigma_c} + 1.5 \right\rfloor} \tag{3.15}$$

where $|f(\xi) - f(x)|$ is the absolute difference of pixel intensities between ξ and x, and σ_c is the combinational range. This is a two-phase procedure and has perfect ability to reduce the impulse noise in images (Huang and Fuh, 2006).

Sharp changes in gradients and large, high-gradient areas degrade the desirable smoothing abilities of the bilateral filter (Paris et al., 2009). The trilateral filter introduced by Choudhury and Tumblin (2003) addressed these problems by combining modified bilateral filters with a pyramid-based method to limit filter extent. In this method, the BF is first applied to the image gradients to estimate the slopes; then the extent of the BF applied to the intensity is skewed according to the slopes. Furthermore, for each output pixel, they apply a threshold to the staircase features to form a binary signal that limits the smoothed neighborhood to connected regions that share similar filtered-gradient values. This approach achieves good performance for denoising polygonal meshes. However, this good performance relies on higher computational cost (Paris et al., 2009).

In summary, though several modifications have been proposed and made an

achievement in different applications in the past years, they still have the weakness and shortcomings, such as time-consuming. Particularly for SAR sea ice images, there is no evidence to show the effectiveness of some of above approaches. As a result, a new modification of BF for SAR sea-ice segmentation is introduced in the next Chapter.

Chapter 4

Methodology

4.1 Flowchart of GBFK Approach

In this project, a two-phase scheme (Kwon et al., 2012) is designed for the segmentation task. The main flowchart of the proposed approach is demonstrated in Fig. 4.1.

In Phase 1, the original SAR images are first denoised as the preprocessing via a Gamma-based bilateral filter (GBF), which consists of two terms: spatial closeness and similarity of intensity. In detail, for the spatial closeness, its parameter is tuned as the coefficient of variation, which is a significant measure of homogeneity in the sliding window; for the similarity of intensity, a new likelihood probability function is exploited instead of Gaussian function based on the fact that the speckle noise in SAR imagery usually follows the Gamma distribution.

In Phase 2, a median filter is adopted in the filtered images as an optional process (mostly used for the simulated images). Then the K-means algorithm with optimized initial centroids of classes is utilized in order to cluster the filtered images into various classes.

Since this two-phase approach includes a Gamma-based Bilateral Filtering and K-means algorithm, it can be named as GBFK in short.

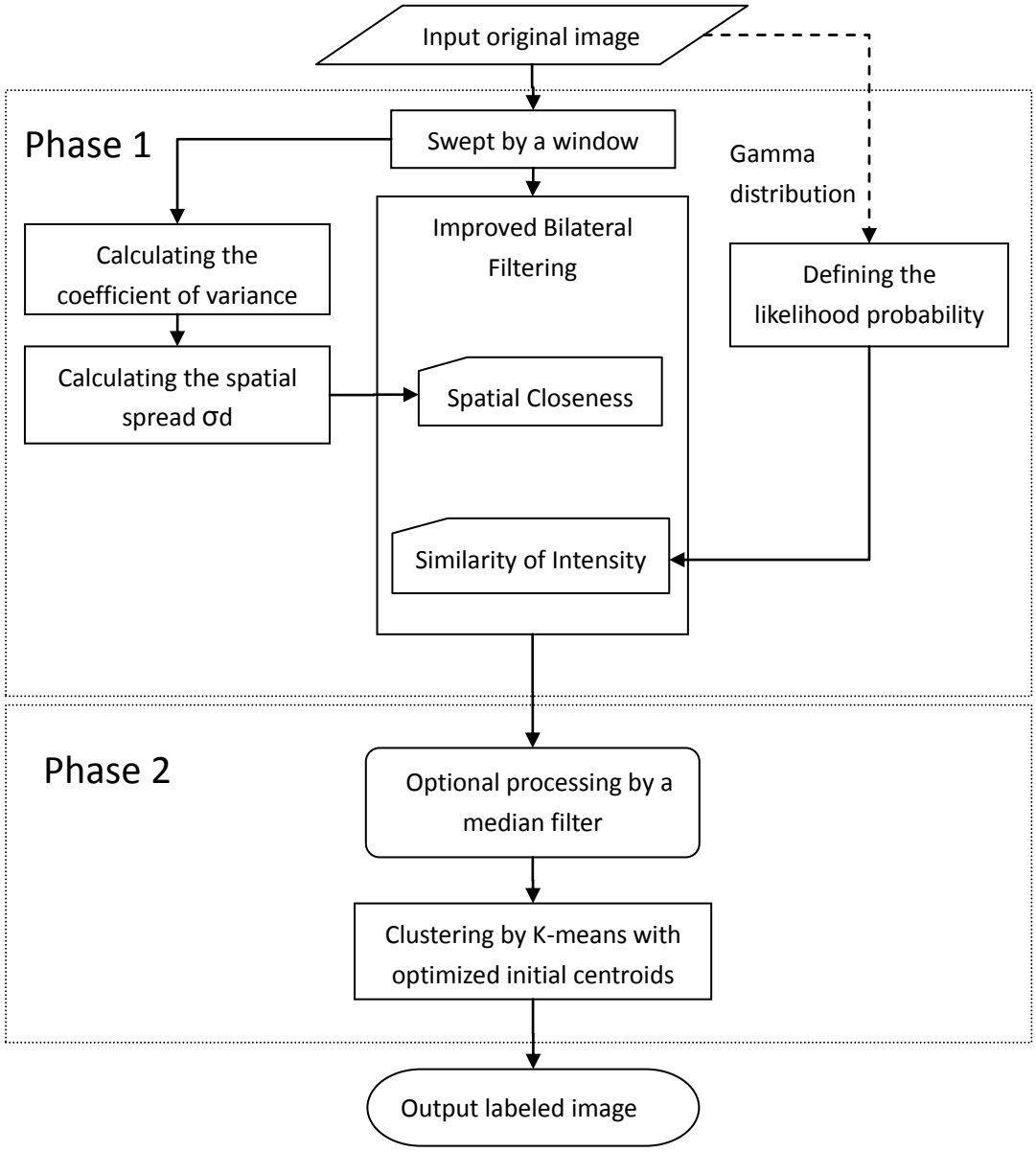

Fig. 4.1 Flowchart of the GBFK approach

4.2 Gamma-based Bilateral Filter

The most critical problem for CBF is how to determine the parameters. To evade this problem, one can just test large number of different parameters and then obtain optimal ones. For instance, after lots of tests, Tomasi and Manduchi (1998) select the parameters by their visual comparison, and Zhang et al. (2009) rely on ENL and ESI indexes. In addition, although several approaches (Zhang and Allebach, 2007; Wong, 2008) discussed in Section 3.3 find a way to determine the parameters adaptively, it is hard to say whether they are effective for SAR sea-ice images.

What is more, when dealing with the SAR images, it is extremely difficult for CBF to achieve satisfied performance by adjusting the two parameters according to my experiments. Speckle noise in SAR images has a great influence on the results. To this end, the similarity of intensity can be described by a likelihood probability function based on Gamma distribution, since the mean square root of speckle noise is usually satisfied unit-mean Gamma distribution (Goodman, 1976). In this section, a new way to modify the CBF is presented as follows.

4.2.1 Spatial Closeness

Since the bilateral filtering has two terms, each of them can be modified separately. For the spatial filter $c(\xi, x)$, most researchers come cross a problem that how to

choose the spatial spread σ_d in Eq. (3.6). For an automatic approach, less parameters that are input by human is expected.

Parameter σ_d determines the shape of the Gaussian curve. Learning from Eq. (3.6), it is obvious that the bigger σ_d is, the lower decreasing rate of $c(\xi, x)$ is as the spatial distance of two pixels decreases; and vice versa. So if σ_d is a constant, a large σ_d may cause relatively large weights of neighborhood resulting in blurring the details, while a small σ_d may cause relatively small weights of neighborhood resulting in bad smoothing ability in homogeneous regions. Hence the selection of σ_d could be significantly relevant to the homogeneity in a region. As we know, the coefficients of variation denoted as C_V is the most commonly used measure of homogeneity, which is given by (Lopes et al., 1990):

$$C_V(x) = \frac{\sqrt{var(f(x))}}{E(f(x))} \tag{4.1}$$

where var(f(x)) and E(f(x)) are variance and mean of pixels in the window respectively. As a result, C_V is utilized to determine the spatial spread σ_d in this project.

Now the problem is how to build up the relationship between σ_d and C_V. Lopes et al. (1990) divide the regions into three classes with two thresholds C_u and C_{max}, based on the regions' homogeneities. For L-look intensity image, Lopes et al. (1990)

recommended that C_u and C_{max} can be given by

$$C_u = \sqrt{\frac{1}{L}} \tag{4.2}$$

$$C_{max} = \sqrt{3}C_u \tag{4.3}$$

where L is the number of looks of SAR images. If $C_V \leq C_u$, then the area denoted as Class 1 should be smoothed; if $C_u < C_V < C_{max}$, then the area denoted as Class 2 should be filtered, containing some textural information; if $C_V \geq C_{max}$, then the area denoted as Class 3 should be preserved, containing more details.

As mentioned above, large spatial spread σ_d blurs more, so a large σ_d works well in homogeneous areas, where a small coefficients of variation C_V exists. Therefore, there is an inverse relationship between σ_d and C_V, so a model for them can be expressed by:

$$\sigma_d(C_V) = \frac{A}{1 + e^{K(C_V - C)}} \tag{4.4}$$

There are three unknown parameters A, K and C to be determined in Eq. (4.4). Two schematic diagrams are demonstrated in Fig. 4.2 in order to clearly and intuitively explain how to determine the parameters. Since $c(\xi, x)$ belongs to [0, 1] after normalization, the median value 0.5 is select as the threshold. Therefore, for Class 1

area, assuming when $\|\xi - x\| \geq \frac{N-1}{2}$, then $c(\xi, x) \leq 0.5$, and the equality is satisfied when $C_V = C_u$, marked as triangle in Fig. 4.2(a); for Class 3, when $\|\xi - x\| \leq 1$, then $c(\xi, x) \geq 0.5$, and the equality is satisfied when $C_V = C_{max}$, shown as ellipse in Fig. 4.2(a). Fig. 4.3(a) shows the curve of the model. The curve is segmented into three parts by two breakpoints: the top part is for Class 1, the bottom part is for Class 3 and the intermediate is for Class 2. Fig. 4.2(b) shows the positive half of Gaussian curve of spatial closeness at two different values of C_V. It is easily observed that when region is smoother ($C_V = C_u$), the Gaussian curve is relatively flatter, meaning that it has stronger power to smooth; and vice versa. Hence, combined with Eq. (3.6), the two equivalent conditions of Class 1 and Class 3 can be described as follows:

$$e^{-\frac{1}{2}\left(\frac{N-1}{2\sigma_d(C_u)}\right)^2} = 0.5 \tag{4.5}$$

$$e^{-\frac{1}{2}\left(\frac{1}{\sigma_d(C_{max})}\right)^2} = 0.5 \tag{4.6}$$

In addition, assuming that the model in Eq. (4.4) is symmetric, we can get:

$$\sigma_d(C_u) + \sigma_d(C_{max}) = A \tag{4.7}$$

By integrating Eqs. (4.2) to (4.7), the three unknown parameters can be computed as following:

$$A = \frac{N - 1}{2\sqrt{-2\log 0.5}} \tag{4.8}$$

$$K = \frac{2\log\frac{2}{N-1}}{C_u - C_{max}} \tag{4.9}$$

$$C = \frac{C_u + C_{max}}{2} \tag{4.10}$$

In final, the new spatial closeness is defined as:

$$c(\xi, x) = e^{-\frac{1}{2}(\frac{\|\xi - x\|}{\sigma_d(C_V)})^2} \tag{4.11}$$

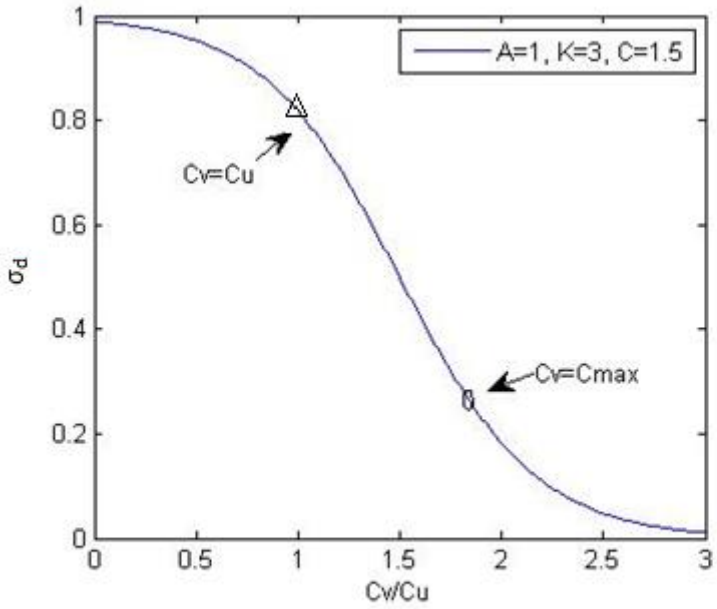

(a) Cv versus σ_d

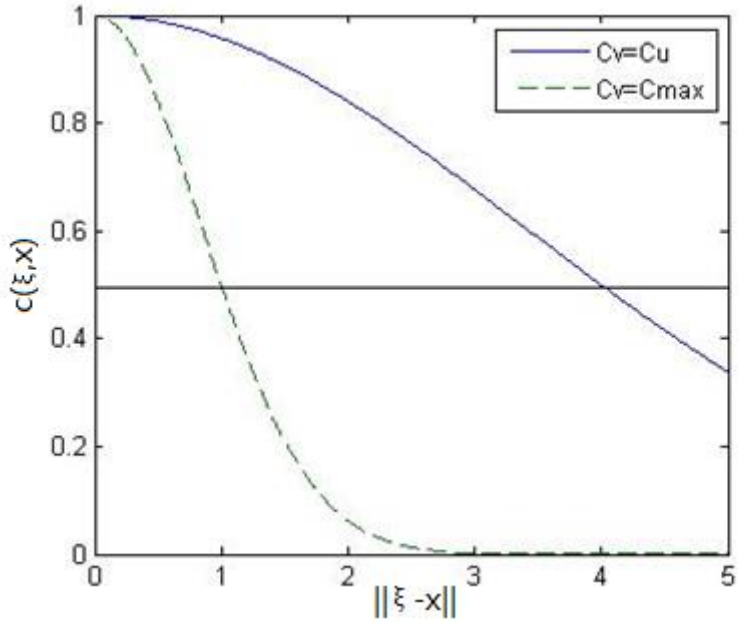

(b) $\|\xi - x\|$ versus $c(\xi, x)$

Fig. 4.2 Schematic diagrams for determining the parameters

4.2.2 Similarity of Intensity

Gaussian function is commonly used to describe noise in image processing, including CBF. However, it can be applied for the spatial filter reasonably but not for the range filter.

On the one hand, Gaussian function cannot deal with the convex impulse noise. According to Huang et al. (2006), CBF by Tomasi and Manduchi (1998) cannot deal with the impulse noise (shown in Fig. 4.3). The range weight will contribute more in this case. In fact, the similarity of intensity will achieve nearly zero weights for

nearby pixels but very high weights for centre pixel if the centre pixel is an impulse. Hence the impulse will remain after filtering. Unfortunately, speckle noise in SAR imagery is also a sort of salt-and-pepper noise that has significant impulse, so CBF based on Gaussian function does not works well. On contrary, Gamma function is able to deal with the convex impulse due to the sharp slope of its curve at [0, 1]. For instance, Fig. 4.4 shows the difference of CBF and GBF when dealing with convex impulse noise. It is obvious that GBF has stronger ability to smooth the convex impulse noise.

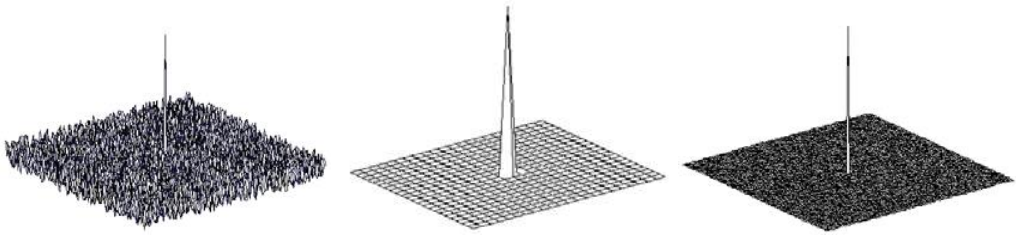

(a) (b) (c)

Fig. 4.3 Disadvantage of the bilateral filter where salt-and-pepper noise remains after bilateral filtering: (a) Impulse noise in a noisy image; (b) Bilateral filter mask at the impulse point; (c) Impulse noise after the bilateral filtering (adapted from Huang et al., 2006)

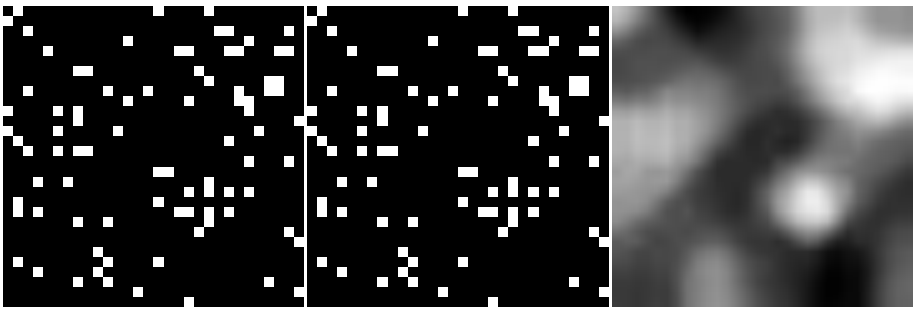

(a) (b) (c)

Fig. 4.4 Difference of CBF and GBF when dealing with convex impulse noise. (a) original image; (b) image filtered by CBF; (c) image filtered by GBF.

On the other hand, researchers often build speckle noise model for SAR imagery via noise with unit-mean gamma distribution (Goodman, 1976; Yu et al., 2009; Kwon et al., 2012). Thus in SAR image segmentation, the use of Gamma distribution presents the better results than Gaussian distribution (Rocha, 2008). For SAR images with number of looks L, probability model of the speckle noise is expressed by Molina et al. (2010):

$$P\left(\frac{f}{g}\right) = \frac{2L^L}{\Gamma(L)}\left(\frac{f}{g}\right)^{2L-1} e^{-L\left(\frac{f}{g}\right)^2} \tag{4.12}$$

where g is noise-free pixels, and f is observed pixels.

A typical equation defining the probability density function of a Gamma-distributed random variable x is:

$$f(x; k, \theta) = \frac{1}{\theta^k}\frac{1}{\Gamma(k)}x^{k-1}e^{-\frac{x}{\theta}} \tag{4.13}$$

where k and θ are shape and scale parameters, respectively. Under the unit-mean condition, θ can be expressed by:

$$\theta = \frac{1}{k} \tag{4.14}$$

thus Eq. (4.13) can be rewrite as:

$$f(x;k) = \frac{k^k}{\Gamma(k)} x^{k-1} e^{-kx} \tag{4.15}$$

It is easy to see that Eq. (4.15) has similar format as Eq. (4.12), which is in line with the multiplicative property of speckle noise in SAR imagery. As a result, using Gamma distribution may be more appropriate to describe the similarity of intensity for SAR imagery.

In this project, based on the Eq. (4.15), a likelihood probability function for similarity of intensity can be defined as follows:

$$s\big(f(x), f(\xi)\big) = P\big(f(\xi)\big|f(x)\big) = \frac{T^T}{\Gamma(T)} \left(\frac{f(\xi)}{f(x)}\right)^{2T} e^{-T\left(\frac{f(\xi)}{f(x)}\right)^2} \tag{4.16}$$

where x is the current pixel, ξ is the nearby pixel, and T is the parameter. Since Eq. (4.16) is similar as Eq. (4.12), T and L may have simple relationship. In fact, the value of T is not very sensitive to the results. Therefore, in the tests, a linear assumption is made between T and number of looks. By trial and error, T can be calculated by an empirical equation:

$$T = \frac{L}{20} \tag{4.17}$$

where L is the number of looks.

4.2.3 Summary of Denoising Phase

To sum up, the denoising phase can be described as follows:

Input: The original image

Output: The filtered image

Procedure:

1. *Set the size of window N.*
2. *Determine number of looks. If number of looks is unknown, using equivalent number of looks (ENL) to replace (how to calculate ENL is introduced in Chapter 4). Then compute parameter T by Eq. (4.17).*
3. *Integrate Eq. (4.2)~(4.3) and Eq. (4.8)~(4.10) to compute three parameters A, K and C, then get the model Eq. (4.4).*
4. *In each window, estimate the value of central pixels:*
    1) *Calculate the coefficient of variation* C_V *by Eq. (4.1).*
    2) *Calculate* $\sigma_d(x)$ *from* $C_V(x)$ *by using Eq. (4.4).*
    3) *Substitute* $\sigma_d(x)$ *into Eq. (3.6) to get the spatial weight.*
    4) *Incorporate the spatial weight and range weight calculated by Eq. (4.13) to*

obtain the estimated value of central pixel.

4.3 K-means algorithm

In this study, the K-means clustering algorithm is used for SAR sea-ice image segmentation since it is a widely used clustering algorithm and simple to use. Moreover, the K-means clustering algorithm has high computational efficiency.

4.3.1 Typical K-means Algorithm

Regarding the pixels all over the image as the observations X, K-means algorithm aims to partition them into k classes S_i (i = 1, 2, …, k) based on their inherent distance from each other. The key point is to minimize the within-cluster sum of squares expressed by

$$\arg\min_{S} \sum_{i=1}^{k} \sum_{x_j \in S_i} \left\| x_j - \mu_i \right\|^2 \tag{4.18}$$

where μ_i is the centroids or means of points in S_i.

This algorithm can be described as follows:

Input: The filtered image

Output: The labeled image

Procedure:

1. *Set the number of class k.*
2. *Compute the intensity distribution (histogram) of the images.*
3. *Initialize the centroids with k uniform distributed values.*
4. *Repeat the following steps until the class labels do not change any more.*
    a) *Cluster the pixels based on the distance between pixels' intensities and centroids' intensities.*
    b) *Compute the new centroids for each class.*

Note that the K-means algorithm adopted in this study was coded by Herrera (2005). More details in connection with K-means algorithm can be found in Hartigan and Wong (1979).

4.3.2 Optimization of Initial Centroids

The typical K-means algorithm usually selects the initial centroids randomly or uniformly. However, this probably leads to convergence at local minima but not global optimum, so that the performance of K-means greatly relies on the correctness of the initial centroids (i.e. in our experiment, the final centroid can hardly reach the gray value of the new ice for some test images due to less pixels belonging to new ice in these images).

An intelligent optimization method for initializing centroids of K-means is introduced based on *density* and *distance*. In this project, it is adopted instead of initializing uniformly in above K-means algorithm.

First of all, based on the histogram of input image, a new set containing all non-zero number of gray value is built. Then for each gray value in this set, the *density* can be calculated by:

$$P_i = k^{-1} \sum_{j=0, j\neq i}^{n} \frac{1}{|x_j - x_i|} \tag{4.19}$$

where $|x_j - x_i|$ is the absolute difference between gray values x_j and x_i, k is the normalization constant. P_i can measure the density of the *i*th gray value. The bigger p_i is, the more gray values locate near the *i*th gray value; and vice versa. Therefore, the gray value which has the largest p_i can be selected as the first centroid of class.

In addition to concerns about the density, the *distance* of gray values also have to be considered. In detail, the distance between centroids should be as large as possible; otherwise all obtained centroids of classes will be too close. The distance can be expressed by:

$$D_{ij} = k^{-1} \sum_{j=0, j \neq i}^{n} |x_j - x_i| \tag{4.20}$$

where $|x_j - x_i|$ is the absolute difference between gray values x_j and x_i (x_i is the previously selected centroid value), k is the normalization constant. Based on the previous centroid, the new centroid should satisfy the maximum cumulative multiplication of density and distance, which can be expressed as:

$$W_i = P_i \sum D_{ij} \tag{4.21}$$

where *i* denotes the number of the previous centroid and *j* denotes the number of new centroid.

In general, this initialization algorithm can be summarized as follows:

Input: The image data

Output: The initial centroids of classes M

Procedures:

1. *Calculate the histogram of input image and extract the non-zero number of gray value as a new set.*
2. *Calculate the density of each gray value in the new set using the Eq. (4.19).*
3. *Initialize the M={ }, and* $W_i = 0$.
4. *Let j=1, choose the first centroid* m_1 *which has the largest* P_i*:*

   $P_1 = max(P_i)$ $(i = 0, 1, 2, \dots, n)$, *then* $M = M \cup \{m_1\}$.

5. *According to Eqs. (4.20) and (4.21), calculate the distance between the previous centroid* m_j *and other gray values, and then compute the* W_i.
6. *Let j=j+1, choose the centroid* m_j *which satisfies:*

   $W_j = max(W_i)$ $(i = 0, 1, 2, \dots, n)$, *then* $M = M \cup \{m_j\}$.
7. *Repeat step 5 to step 6 until setting k centroids of classes.*

4.4 Optional Process

In this study, a median filter (with 3x3 window size) is used for the filtered images for simulated tests, because there exist some dark points remaining after Gamma-based bilateral filtering. The dark points mostly appear in simulated images due to the "zero" pixels. The simulated images are normalized to [0,1] when recorded, so there are some zero pixels on them. Even though a small value has been added to the synthetic images in order to avoid the zero-denominator problem, when the near-zero pixel locates at the centre of window, the ratios of nearby pixels and centre pixel can be extremely large, leading to nearly all weights of nearby pixels tending to zero. Hence the estimate value of centre pixel eventually is determined by itself, that is, almost zero.

For this reasons, the median filter is utilized in the simulation. It is a really suitable one that can preserve boundaries well as a nonlinear filter. Moreover, it can achieve relatively high signal-to-noise ratio (SNR) and in the meantime low computation time

(Huang et al., 2006). On contrary, real SAR images do not have the “zero” pixels, thus without the median filter, results are still satisfying. Therefore, the median filter is not applied in the real SAR data tests, leading to this “optional” process.

4.5 Experimental Design

In this study, two main experiments are implemented based on both simulated images and real SAR images. The purpose of simulation is to make the results derived from the real SAR data more reliable, and to show the robustness of the proposed method under various variances. Of course, three other approaches, including Frost filter followed by K-means (FK), CBF followed by K-means (CBFK) and Maximum Likelihood Classification (MLC), are adopted as comparative approaches. Notice that the parameters of comparative methods are selected by one-at-a-time, in which the best one is visually determined depending on the final labeled results.

4.5.1 Choice of Comparative Approaches

Two other methods, Frost filtering followed by K-means (FK) and Conventional Bilateral Filtering followed by K-means (CBFK), were selected to compare with the proposed method.

First, in this study, denoising or filtering phase plays the most important role, so the FK approach is very proper to be a compared method. It even can be the baseline in the experiments, since the Frost Filter (Frost, 1982) is considered to be among the best filters for SAR imagery (Gagnon and Jouan, 1997; Touzi, 2002; Leeuw and Carvalho, 2009). In addition, CBFK, of course, should become a comparison since the GBFK is based on it.

4.5.2 Test Design Using Simulated Data

A. Creation of Simulated Image

A clean image, i.e. image shown in Fig. 4.5 consisting of three different classes with irregular edges, is degraded by speckle noise to simulate SAR sea-ice images. The gray values of three classes are set as 30, 110 and 150 degree resulting from that they represent new ice, gray ice and first-year ice, respectively. The relatively small difference between 110 and 150 gray tones can be a challenge of the discriminative ability of segmentation techniques. In this experiment, the simulated images are created by adding Gamma-distributed noise, meaning that the mean squared root (MSR) of speckle noise satisfies Gamma distribution with unit-mean (Goodman, 1976).

Commonly, the SAR image f can be modeled as multiplication of noise-free image g and noise n (Touzi, R., 2002) as follows:

$$f = g * n \tag{4.22}$$

And the noise follows the Gamma distribution, described by Eq. (4.12). In detail, the images are degraded with different levels of speckle noise from L=14 to L=2 step by step, corresponding to variances from σ^2=0.071 to σ^2=0.500.

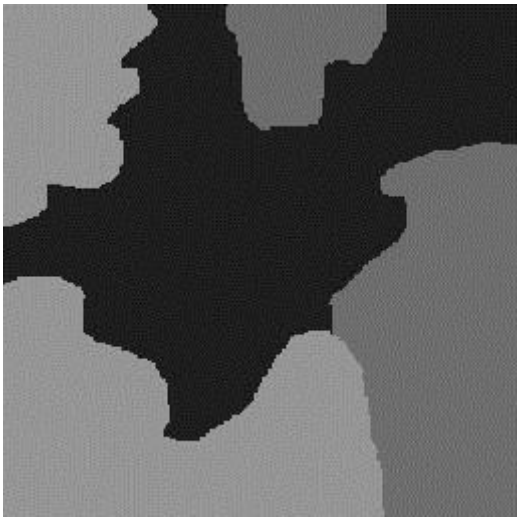

Fig. 4.5 Original synthetic image with 30, 110 and 150 gray level

B. Selection of Parameters

As controlled experiments, their parameters are selected by one-at-a-time, especially for the CBF. Table 4.1 shows the parameters of various filters in tests using simulated images. For all three filters, window size has a significant influence on the filtered results. Considering the total image size, the size of interests and the computational time, the same 7x7 window is chosen for all three filters. In addition, for the Frost Filter, damping factor defines the extent of exponential damping. The smaller the

value is, the better the smoothing ability and filter performance. Hence it is set up as the smallest and commonly used value: 1. Furthermore, for the CBF, a simulated noise image (L=5) is selected to determine the parameters. The spatial spread σ_d should correspond to the local window size and the photometric spread σ_r should correspond to the difference in the range (Tomasi and Manduchi, 1998). Therefore, σ_d is initially set as half of window size: 3, then σ_r is changed from 0.1 to 1 step by step with a 0.1 interval. As a result, σ_r=0.5 leads to a satisfying result based on visually detection. Afterwards σ_r=0.5 is made a constant, and σ_d is changed from 0.5 to 5 step by step with a 0.5 interval. The result shows that the values of σ_d that are bigger than 3 yields similar and satisfying labeled images, so σ_d=3 is selected because the smaller one can preserve more details.

Table 4.1 Parameters of various filters in tests using simulated images

Filters	Parameters
Frost	7x7 window, damping factor K=1
CBF	7x7 window, σ_d=3, σ_r=0.5
GBF	7x7 window

4.5.3 Test Design Using Real SAR Data

The real SAR image used to test the proposed method is a RADARSAT-2 image with several sea-ice types provided by CIS, as shown in Fig. 4.6. The image covers the sea

area nearby the Island of Newfoundland in Canada, and it was taken in HH polarization under ScanSAR Wide beam mode at 22:29:36 on March 16, 2009. Its spatial resolution had been degraded to 100m to enhance sea-ice types. The CIS website provides daily regional ice charts which can help interpret the ice concentration and distributions (see Fig. 2.1).

Four sub-images denoted by R1, R2, R3 and R4 respectively, whose information is shown in Table 4.2, were chosen to test segmentation techniques (shown in Fig. 4.7). In this study, the number of class is considered *a prior* knowledge. R1 consists of new ice and first-year ice, the boundaries between which are easy to be discriminated. R2 has the same ice types but the boundaries are not very clear. Both R3 and R4 include three ice types: new ice, gray ice and first-year ice. In detail, there are only a little new ice areas in R3, which makes a trouble to discriminate the new ice class. As to R4, the boundaries between gray ice and first-year ice are so blurred that it is even difficult to depict them manually.

B. Selection of Parameters

For the bilateral filter, selection of parameters is the same as that in the simulation. Table 4.3 lists the best parameters for three approaches in this study. Notice that the window size of Frost filter is 5x5. The reason is that it is able to preserve more details while still keep good smoothing ability than 7x7 window size.

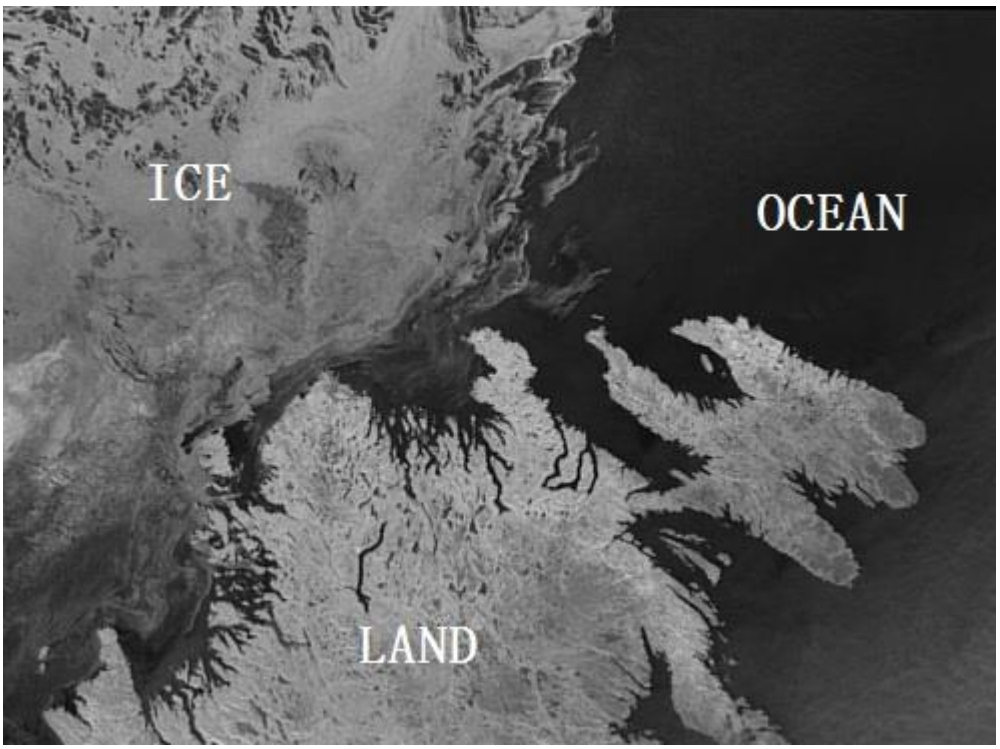

Fig. 4.6 RADARSAT-2 sea-ice imagery in HH polarization under ScanSAR Wide beam mode at 22:29:36 on March 16, 2009 (CIS, 2009)

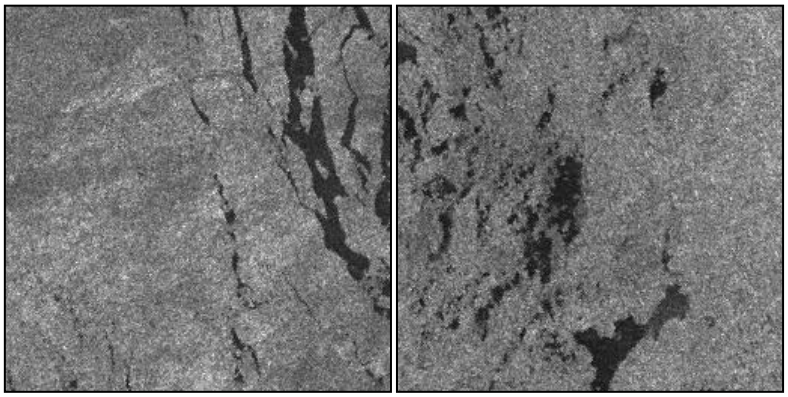

R1 R2

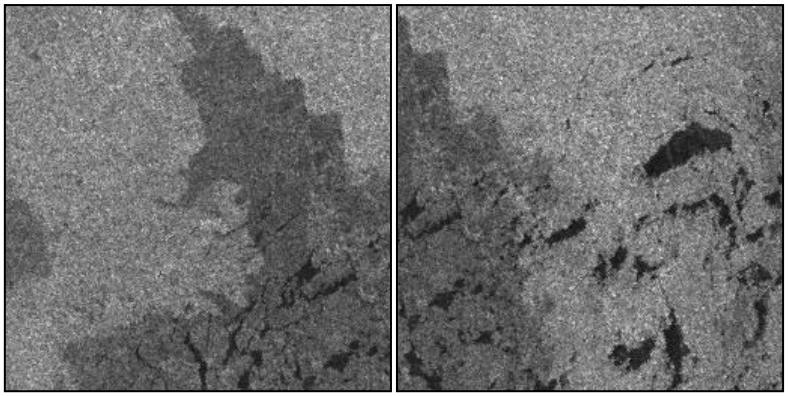

R3 R4

Fig. 4.7 Four subsets of original SAR image

Table 4.2 Summary of tested images

Test Site	Size (pixels)	Number of sea ice types
R1	256×256	2 (Gray sea ice & Medium first-year sea-ice)
R2	256×256	2 (Gray sea ice & Medium first-year sea-ice)
R3	256×256	3 (Gray sea ice, Medium first-year sea-ice & new ice)
R4	256×256	3 (Gray sea ice, Medium first-year sea-ice & new ice)

Table 4.3 Parameters of various filters in tests using real SAR sea-ice images

Filters	**Parameters**
Frost	5x5 window, damping factor K=1
CBF	7x7 window, σ_d=3, σ_r=0.2
GBF	7x7 window

Chapter 5

Experimental Results and Discussion

5.1 An Overview

In this study, both simulated and real SAR images with different sea-ice types are used to test the proposed method. In simulated tests, clean image with ice-like gray tone is degraded by speckle noise whose number of looks range from 14 to 2. Such a large range is able to validate the effectiveness and robustness of the proposed approach. Indeed, F1 score is used to calculated the accuracy of methods for each class. It can directly reflect how accuracy the tests are at various variances. For real SAR images, the true labels are determined by visual interpretation based on prior information provided by ice chart. After segmentation, several statistics are calculated from the confusion matrix to evaluate the results. Instead of using the Kappa indices, the allocation disagreement and quantity disagreement (Jr et al., 2011) is adopted, which were proved being more interpretable and more capable of revealing the sources of errors than Kappa indices. Allocation disagreement results from the mismatch between estimated labels and true labels in the spatial location, while quantity disagreement is the mismatch in the proportion of categories. Furthermore, the overall accuracy is also used as a measure of proportion of pixels that are correctly classified.

5.2 Results Using Simulated Images

5.2.1 Visually Performance Evaluation

A. Segmentation Results

The results of different segmentation methods are shown in Fig. 5.1. It can be easily seen from the first column in Fig. 5.1 that using K-means alone failed to obtain expected results due to the sensitivity of speckle noise. Moreover, visually evaluation on results in Fig. 5.1 suggests that FK, CBFK and GBFK perform the similar results (GBFK slightly outperforms the other two), and there are more and more unexpected spots in the results as the variance of noise increases. This phenomena result from the K-means clustering algorithm, which has poor ability to distinguish the classes whose tones are close.

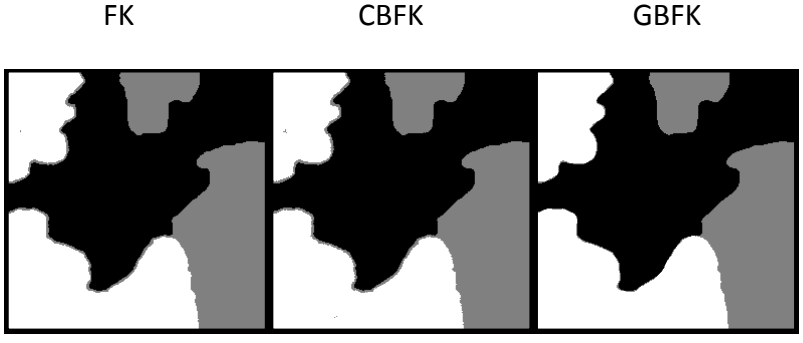

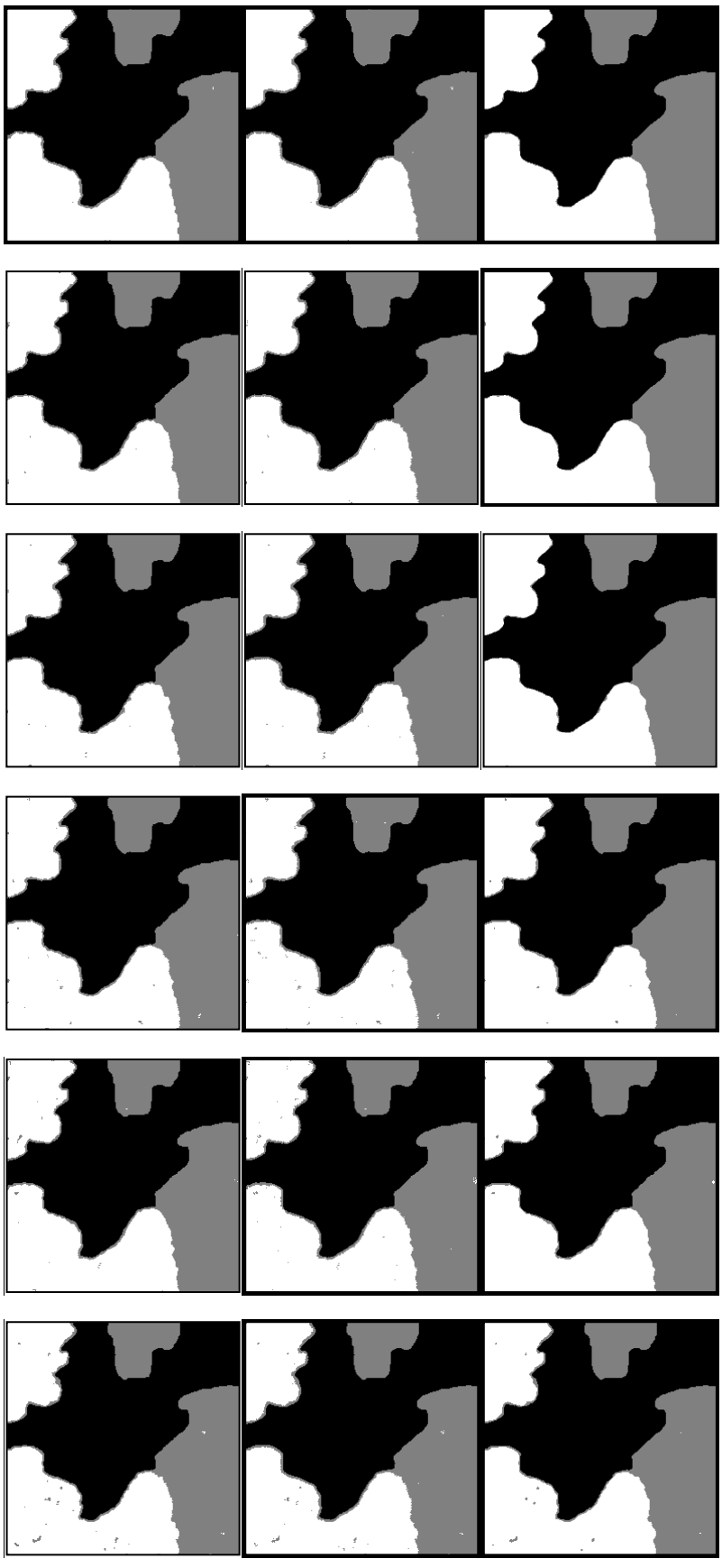

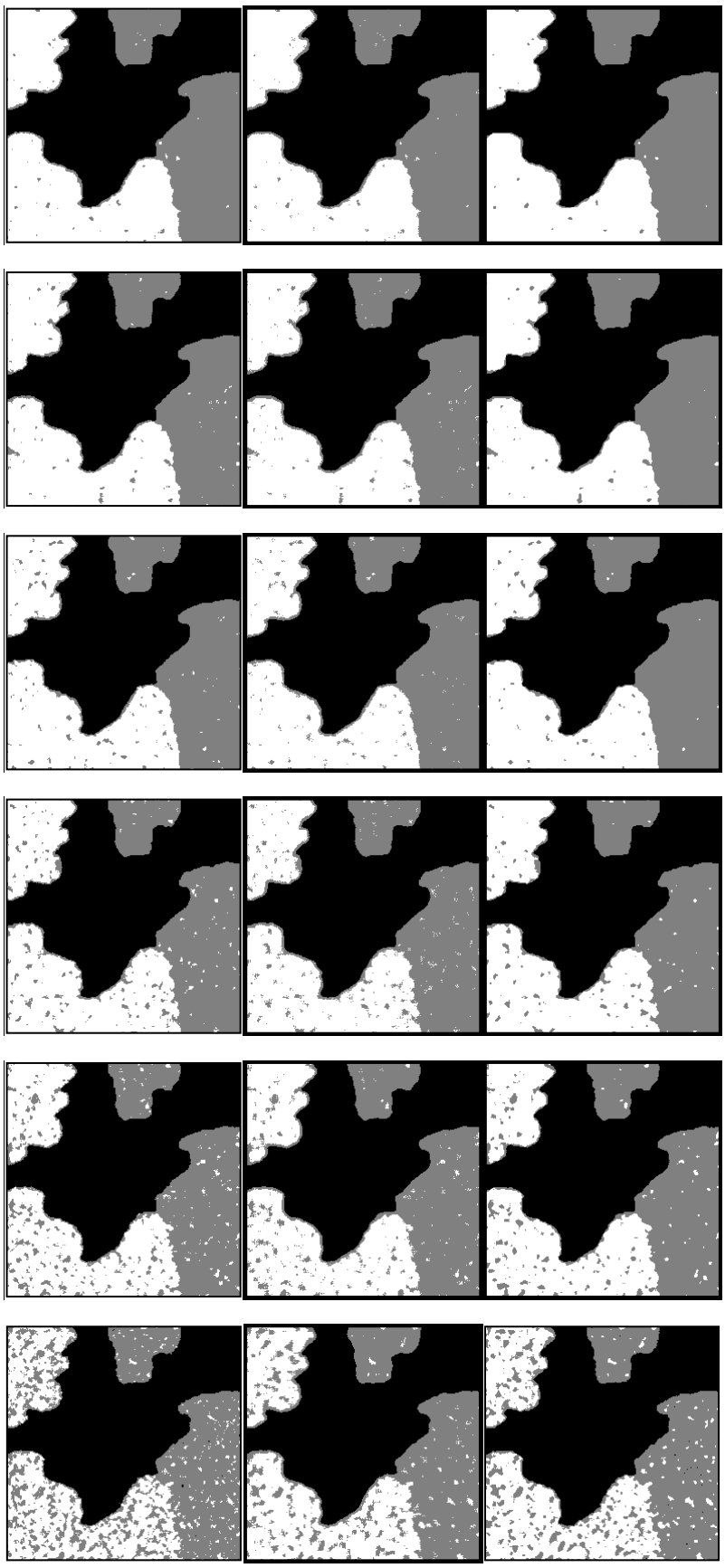

Fig. 5.1 Segmentation results for simulated images added noise with number of looks

from L=14 to L=2 (rows from top to bottom), using FK, CBFK and GBFK respectively (columns from left to right)

B. Filtering Results

To further validate the power of GBF for suppressing speckle noise in SAR images, a synthetic image added speckle noise at L=5 is selected to be tested, shown in Fig. 5.2. In Figs. 5.3-5.5, there are filtered results and their corresponding intensity histograms by applying the Frost filter, CBF and GBF, respectively. Their parameters are shown in Table 5.1. It is observed that there are three clear peaks in histogram in Figs. 5.3-5.5 whereas just two in Fig. 5.2(b), meaning that all the three methods have the ability towards discerning the two classes that have close gray tones. Among these filters, Frost filter and CBF show stronger smoothing power than GBF, whereas GBF preserves edges better than the others.

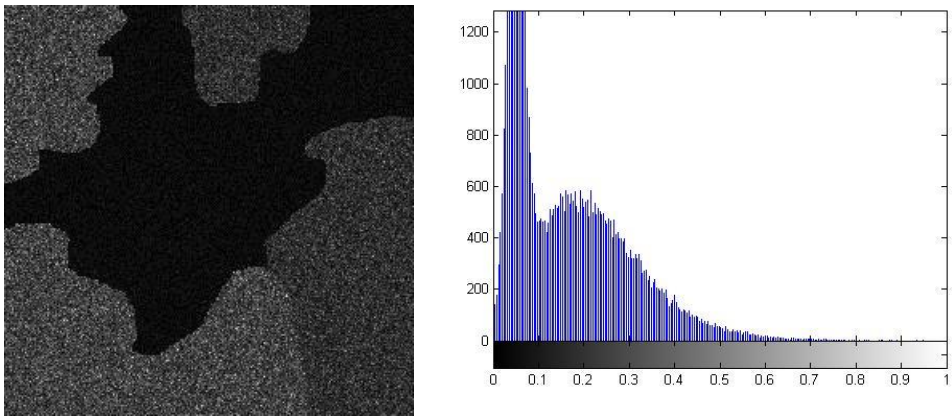

(a) (b)

Fig. 5.2 (a) Simulated noisy image (L=5), (b) its histogram.

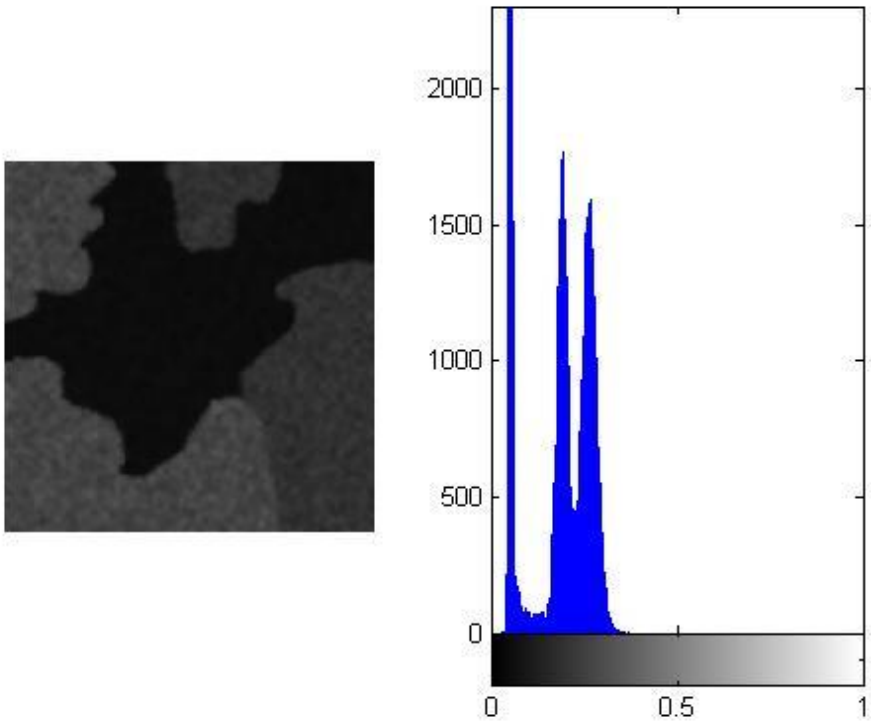

Fig. 5.3 Filtered image and its histogram via Frost filter

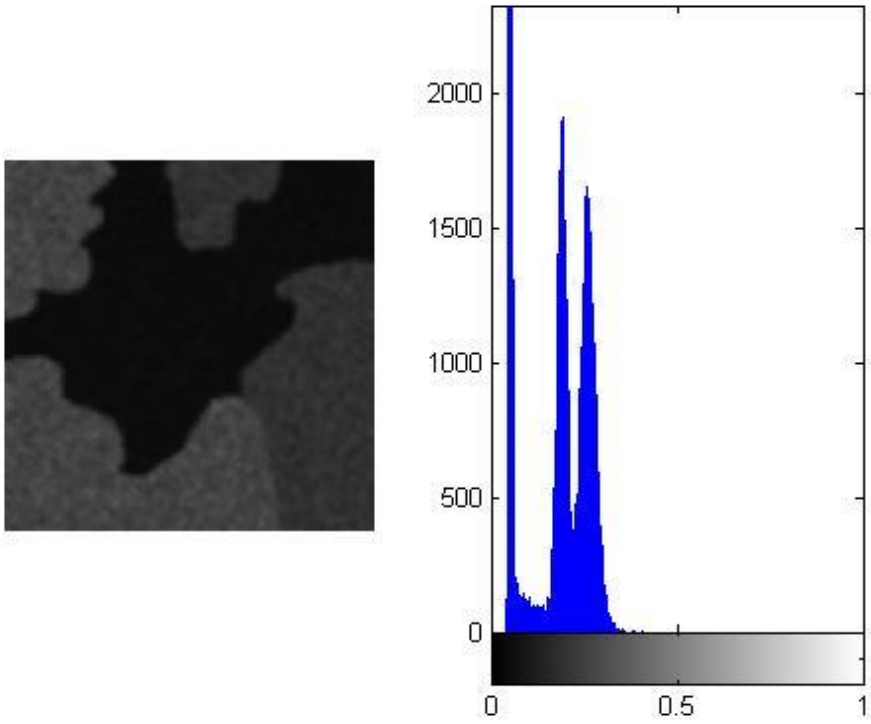

Fig. 5.4 Filtered image and its histogram via CBF

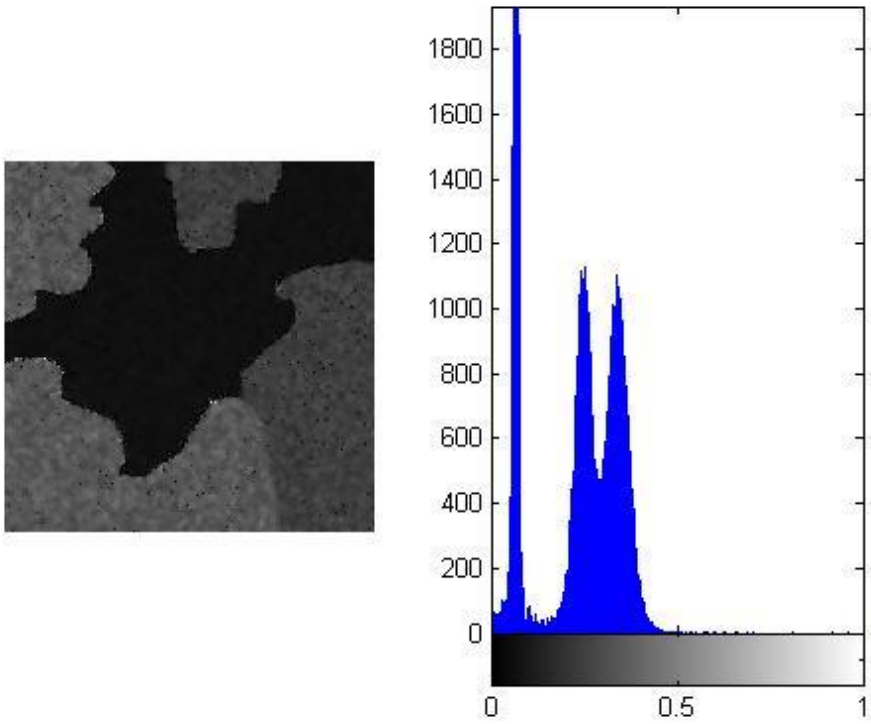

Fig. 5.5 Filtered image and its histogram via GBF

5.2.2 Quantitative Performance Evaluation

Besides visual inspection in Fig. 5.1, quantitative results are shown in Figs. 5.6-5.8. F1 score test is performed, which is widely used to validate the accuracy of test data, in order to find out how each test method performs under different circumstances (in our case, different test methods and noise levels). In other words, within only one figure, it is easy to show how the approaches work for each class under different variances via F1 score. The general equation for F1 score derived based on Rijsbergen's (1979) effectiveness measure can be expressed by:

$$F1 = \frac{2TP}{2TP + FN + FP} \tag{5.1}$$

where TP, FN and FP denote true positive, false negative and false positive respectively. Since there are three classes in test images, three various figures should be drawn so as to observe how accurately the segmenting result of each class is matched to the ground truth image (derived from original synthetic image in Fig. 4.5). The F1 score ranges from zero to one corresponding to the poorest and the best match pattern.

For the other three approaches, the F1 scores of FK, CBFK and GBFK are all higher than 0.8, indicating that these three methods can reduce the speckle noise effectively. Particularly Fig. 5.6 illustrates the F1 score of "new ice" class, in which all other three techniques achieved very high level of scores due to the big difference between the gray values of new ice and other ice. In detail, GBFK algorithm outperforms the others because it uses Gamma distribution to measure the similarity of intensity.

As to the rest two classes shown in Figs. 5.7 and 5.8, F1 score of the proposed method still outperforms the others. Furthermore, it is easily observed that FK performs slightly better than CBFK when the variance of noise is below 0.25. However, as the variance of noise increases, the F1 scores of FK increasingly drop away from CBFK. This demonstrates BF can perform better than the Frost filter at high-level noise. In

the mean time, it can be predict that the F1 scores of CBFK will beyond GBFK as the variance of noise keep increasing, but it is meaningless when the variance of noise is too high.

To sum up, almost all F1 scores of GBFK for each class are higher than 0.9 regardless of the variances of noise, and beat FK and CBFK completely. Since the effect of improvement of BF can be seen, one reason for this is that the constant spatial spread cannot fit various level of speckle noise, while the other reason is that applying difference of gray tones as the measure of Gamma model is more appropriate than using ratio of gray tones as the measure of Gaussian model for the range filter.

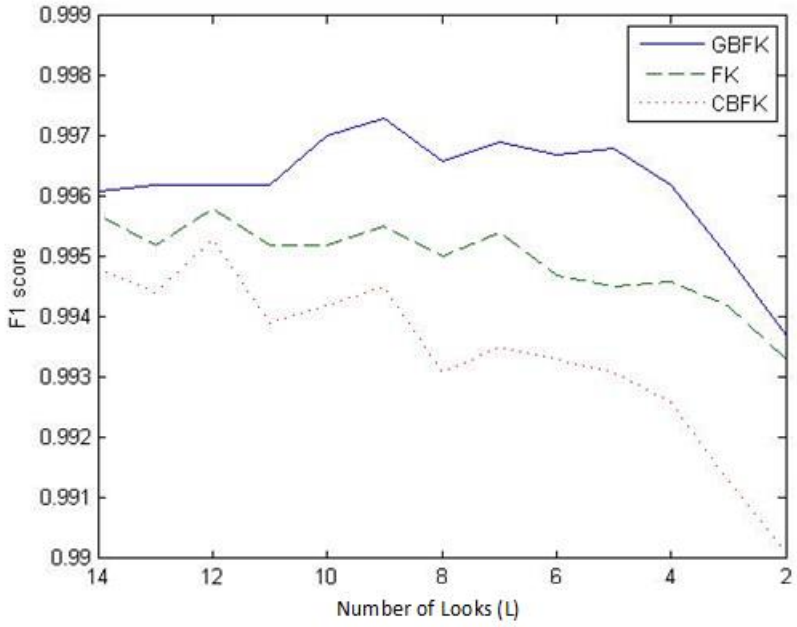

Fig. 5.6 F1 score versus number of looks (L) for new ice class

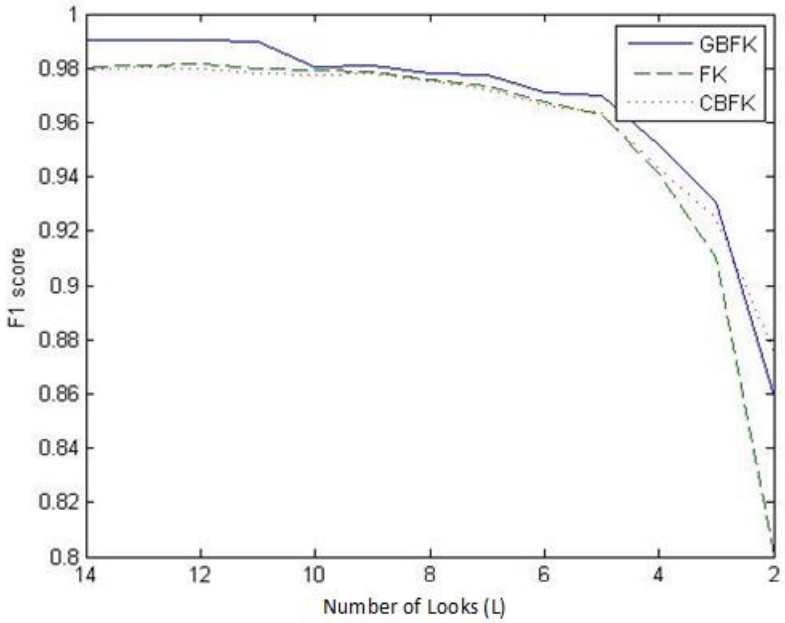

Fig. 5.7 F1 score versus number of looks (L) for first-year ice class

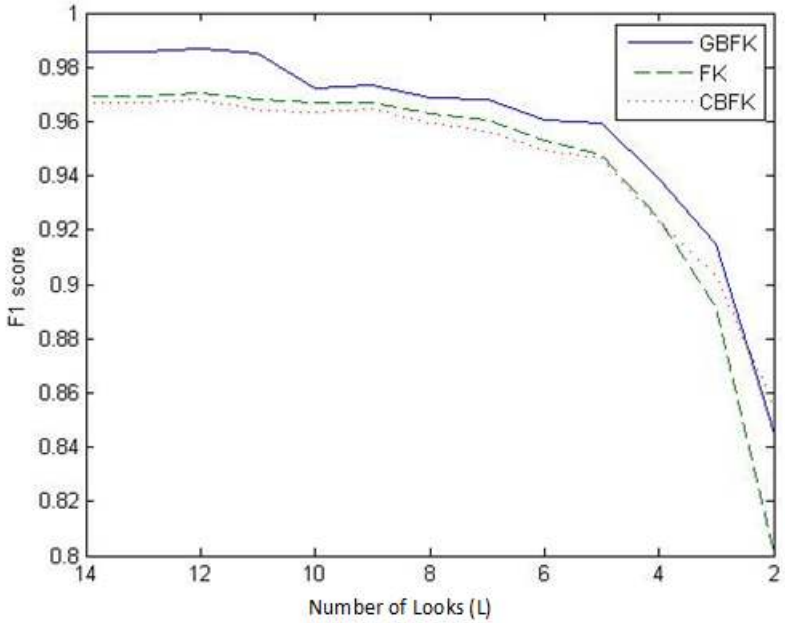

Fig. 5.8 F1 score versus number of looks (L) for gray ice class

5.3 Results with Real SAR Sea-Ice Images

5.3.1 Visually Performance Evaluation

A. Segmentation Results

The four subsets were delineated manually according to their differences of gray tone values, shown in Fig. 5.9. The segmentation results are treated as ground truth. Meanwhile in Fig. 5.10, the overlay segmentation results can be generated by GBFK approach using the parameters shown in Table 4.3. It can be found that even a very small segments can be delineated using the proposed method according to Fig. 5.10. More details will be discussed later based on the labeled images.

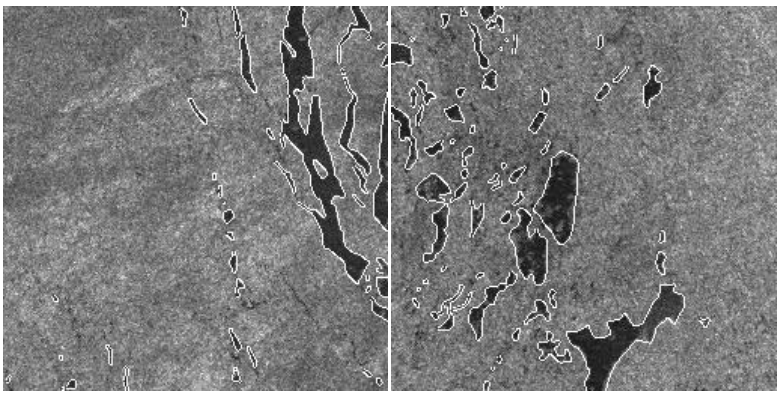

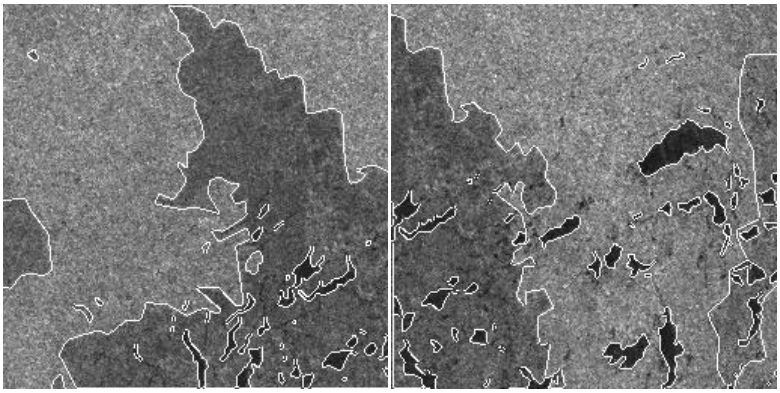

Fig. 5.9 Manully digitized segmentation results

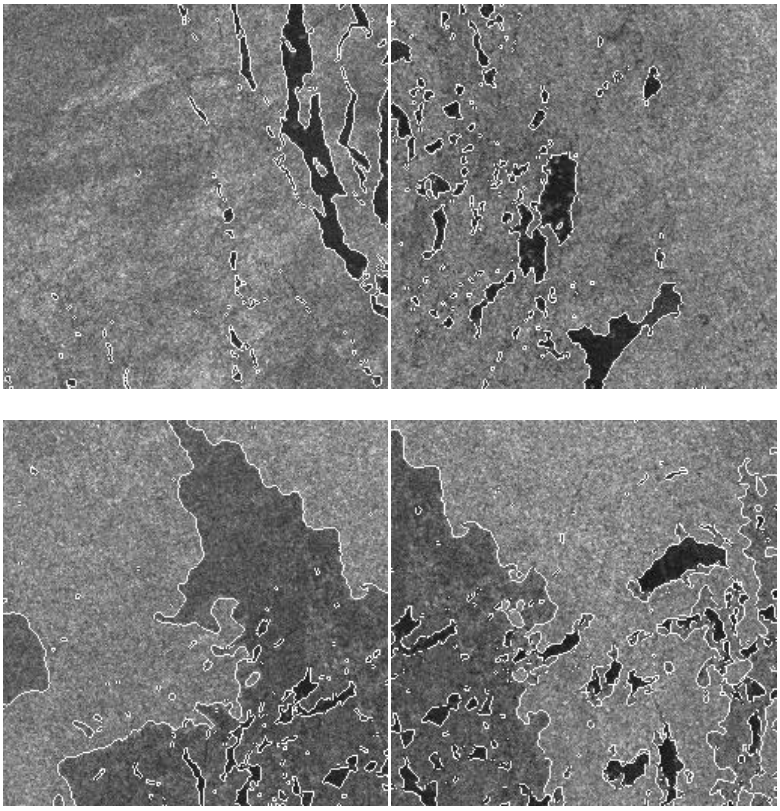

Fig. 5.10 Overlay segmentation results using the proposed method

The experiments on real SAR sea-ice images demonstrated consistent results with the simulated study. It is evident that the proposed GBFK algorithm outperforms the rest algorithms by visual inspection according to Fig. 5.11.

First, according to the simulations, FK and CBK tend to blur the boundaries, so the new ice in Figs. 5.11(a), (b), (e), (f) looks bloated, especially for R2. However, the window size of Frost filter and photometric spread of CBF cannot be turned to small, because if so, their ability to suppress noise will decline rapidly. On contrary, it is easy to find a proper parameter T for GBFK so as to distinguish the new ice more accurately, which results from both the adaptive spatial spread and the range filter based on Gamma distribution.

Secondly, when looking at three-class situation, the proposed GBFK method still outperforms the others. Since new ice in R3 occupies significantly less areas than gray ice and first-year ice, FK and CBFK run into disaster by misclassifying a lot of area of gray ice into new ice, shown in Figs. 5.11(c) and (g). On the other hand, GBFK can achieve satisfied result (Fig. 5.11(k)) as a result of the Gamma-distributed range filter. It has greater ability to preserve edges, thus the K-means algorithm could discriminate the new ice correctly.

Finally, the same problem occurs for R4 using FK and CBFK according to Figs. 5.11(d) and (h), that is, some gray ice is misclassified to new ice. Since the difference of gray value between new ice and other ice is large, the Frost filter and CBF tends to blur the “sharp” edges between new ice and other ice. On contrary, in Fig. 5.11(l), the “sharp” edges are preserved well due to the range filter based on Gamma distribution.

Therefore, using Gamma function to replace Gaussian function for the range filter is effective and necessary in SAR image segmentation.

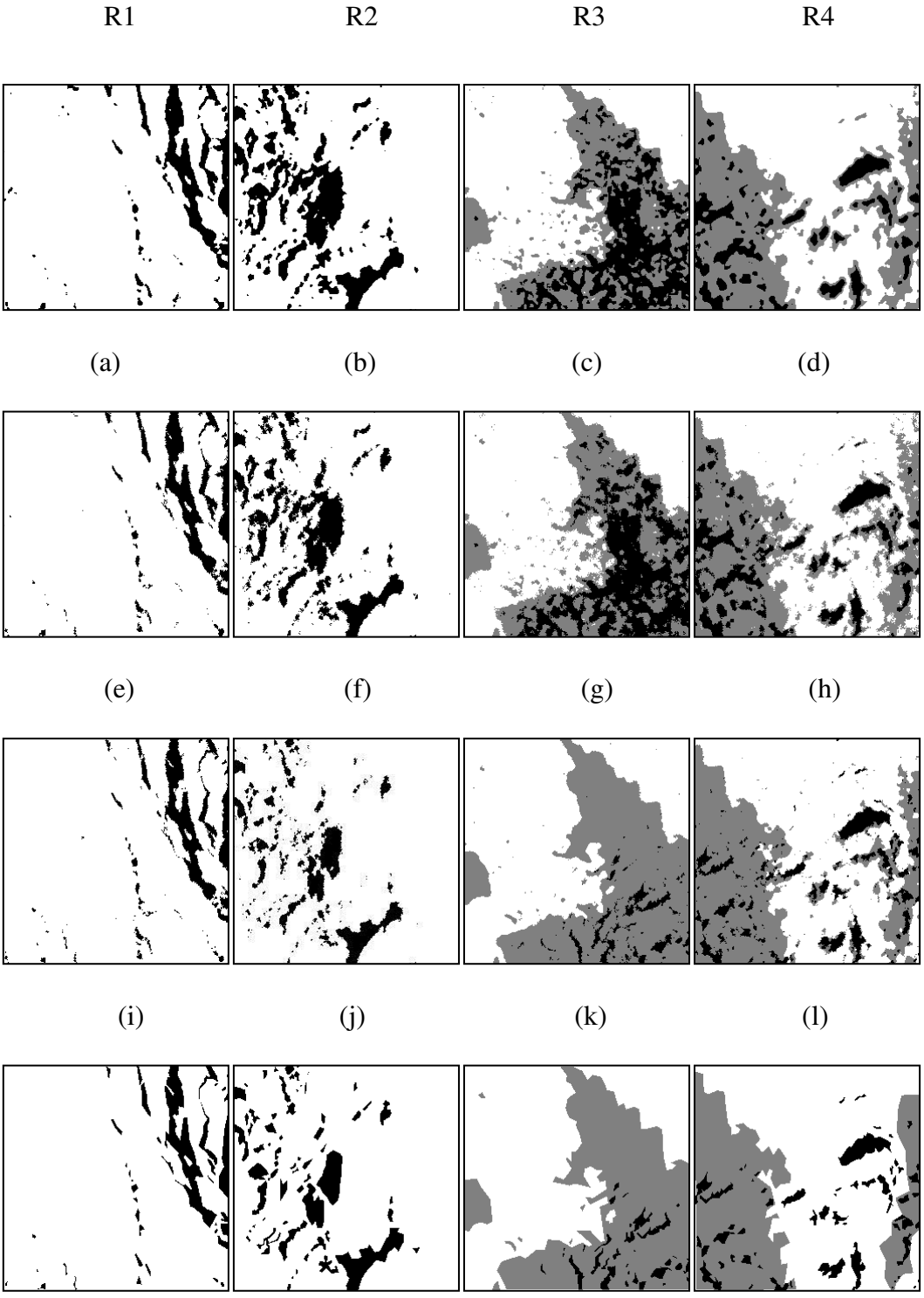

(m) (n) (o) (p)

Fig. 5.11 Segmentation results for real SAR images for R1, R2, R3 and R4 (columns from left to right), using FK, CBFK and GBFK respectively (rows from top to bottom except the last row); the ground truth images are shown in the last row.

B. Filtering Results

Fig. 5.12 shows the filtered results using FK, CBFK and GBFK. It is easy to see that the boundaries by GBFK are clearer and sharper than another two when comparing the filtered images in the same row. Therefore, the improvement of the proposed method exactly makes a difference. Furthermore, according to the histograms, the proposed GBFK approach demonstrates more power to delineate various classes, especially the small class such as new ice class. The satisfying results should mainly be attributed to the Gamma distribution that used as the similarity of intensity. Of course, the adaptive spatial filter is also helpful for preserving edges.

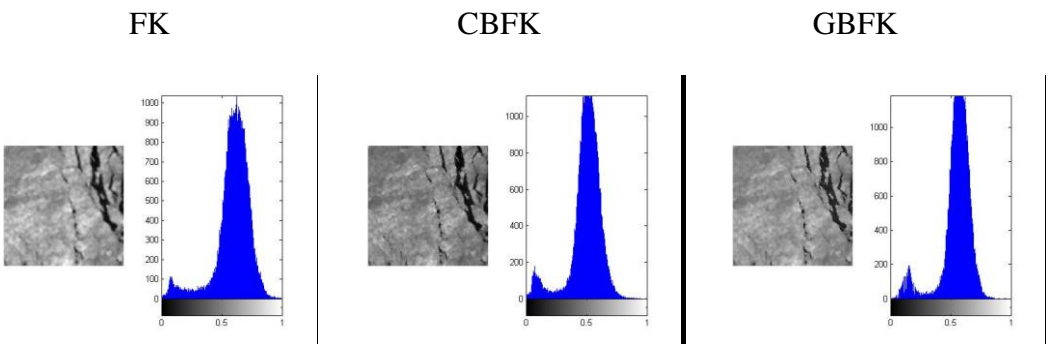

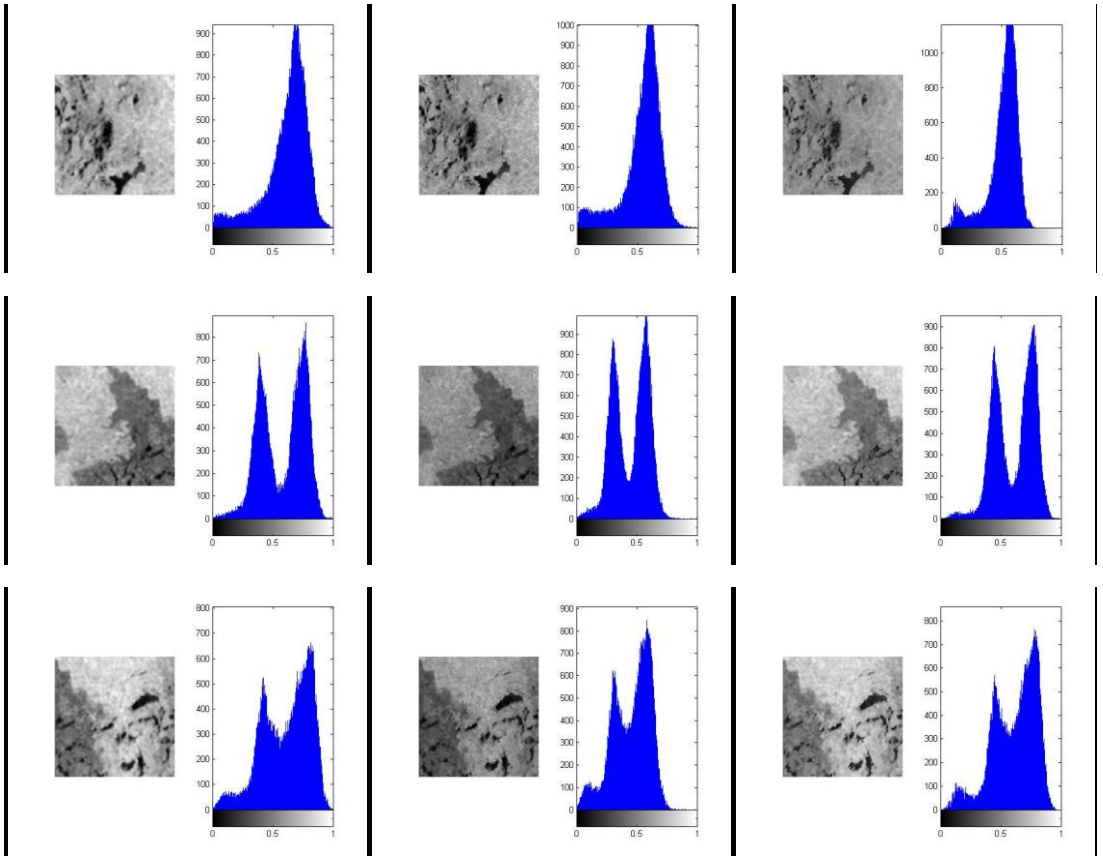

Fig. 5.12 Filtered results and their histograms using FK, CBFK and GBFK (from left to right) for R1, R2, R3 and R4 (from top to bottom)

5.3.2 Quantitative Performance Evaluation

What is more, a statistical analysis is presented in Table 5.1, in which the disagreements and overall accuracy are presented. The disagreement indexes proposed by Jr et al. (2011) are based on the confusion matrix (or error matrix). Let n_{ij} denotes the number at the *i*th row and *j*th column in the confusion matrix. Then the new entry p_{ij} can be expressed by:

$$p_{ij} = \frac{n_{ij}}{N} \tag{5.2}$$

where N is the total number of pixels. The quantity disagreement q_g for an arbitrary category g can be computed by:

$$q_g = \left| \sum_{i=1}^{J} p_{ig} - \sum_{j=1}^{J} p_{gj} \right| \tag{5.3}$$

where J is the number of classes. Then the overall quantity disagreement can be calculated by:

$$Q = \frac{1}{2} \sum_{g=1}^{J} q_g \tag{5.4}$$

The allocation disagreement a_g can be computed by:

$$a_g = 2\min\left(\sum_{i=1}^{J} p_{ig} - p_{gg}, \sum_{j=1}^{J} p_{gj} - p_{gg} \right) \tag{5.5}$$

Thus the overall allocation disagreement is:

$$A = \frac{1}{2} \sum_{g=1}^{J} a_g \tag{5.6}$$

The total disagreement can be calculated by:

$$D = Q + A \tag{5.7}$$

The overall accuracy can be computed by:

$$OA = \sum_{g=1}^{J} p_{gg} \tag{5.8}$$

For an intuitive sense, the disagreement and the overall accuracy diagrams are shown

in Figs. 5.13 and 5.14. In general, the statistical analysis demonstrates a consistent conclusion as the visually evaluation. It is easy to find that the proposed GBFK method performs the best disagreement indexes and overall accuracy for each image; particularly for R3 and R4, it has a significant excellence over the others. From Table 5.1, GBFK achieves average disagreement of 0.0406 and average overall accuracy of 95.62%. Its results are approximately from 6.7% to 15.1% better than other approaches in terms of average overall accuracy. From the Fig. 5.13, it is easily observed that both quantity and allocation disagreements of GBFK are lower than those of compared approaches. Furthermore, GBFK shows a big excellence in quantity disagreement over the others, because quantity disagreement shows more about the results' accuracies. Notice that the FK and CBFK fail to discriminate the new ice class in R3, so their disagreements are significantly large accordingly.

To sum up, the statistical analysis also indicates the proposed GBFK approach can achieve satisfied performances for SAR sea-ice segmentation. Of course, its effectiveness should satisfy some computing time. However, its good performance makes this satisfy accessible.

Table 5.1 Quantity disagreement (Q), allocation dissgreement (A), total dissagreement (D) and overall accuracy (QA) of segmentation results for real SAR images

R1	*GBFK*	*FK*	*CBFK*	**R2**	*GBFK*	*FK*	*CBFK*
Q	0.0050	0.0189	0.0093		0.0116	0.0682	0.0442

A	0.0050	0.0069	0.0088		0.0105	0.0094	0.0166
D	**0.0100**	**0.0257**	**0.0181**		**0.0221**	**0.0776**	**0.0608**
OA	**98.5%**	**97.43%**	**98.19%**		**96.74%**	**92.24%**	**93.92%**
R3				**R4**			
Q	0.0052	0.1643	0.1732		0.0337	0.0679	0.0627
A	0.0320	0.0362	0.0362		0.0594	0.0834	0.0772
D	**0.0372**	**0.2005**	**0.2110**		**0.0931**	**0.1513**	**0.1399**
OA	**96.28%**	**79.95%**	**78.9%**		**90.69%**	**84.87%**	**86.01%**

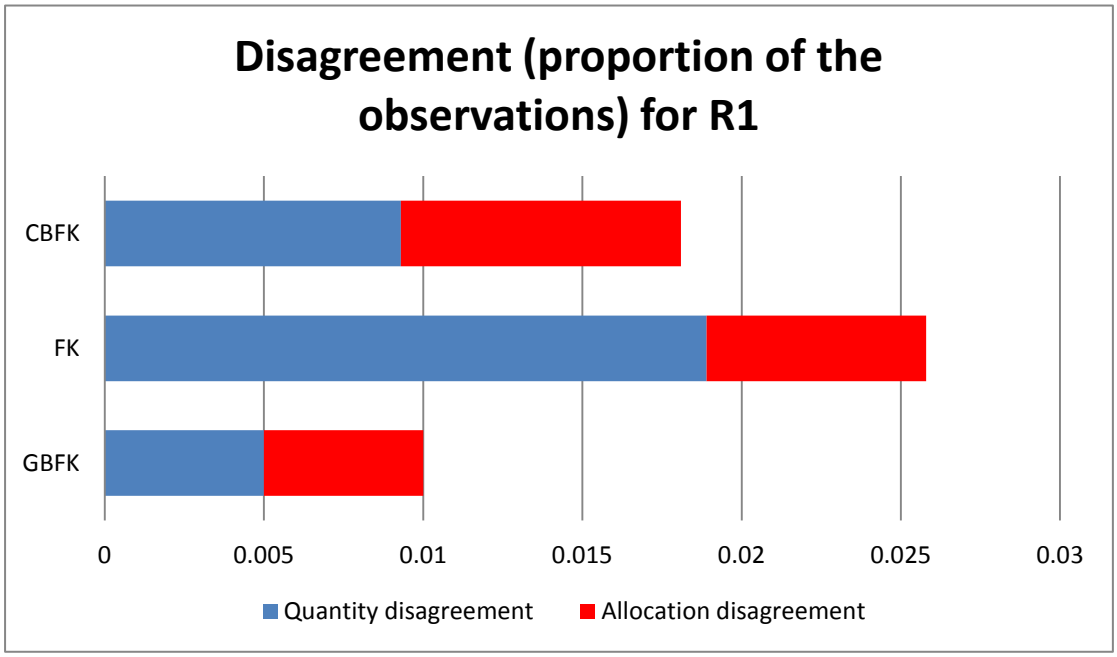

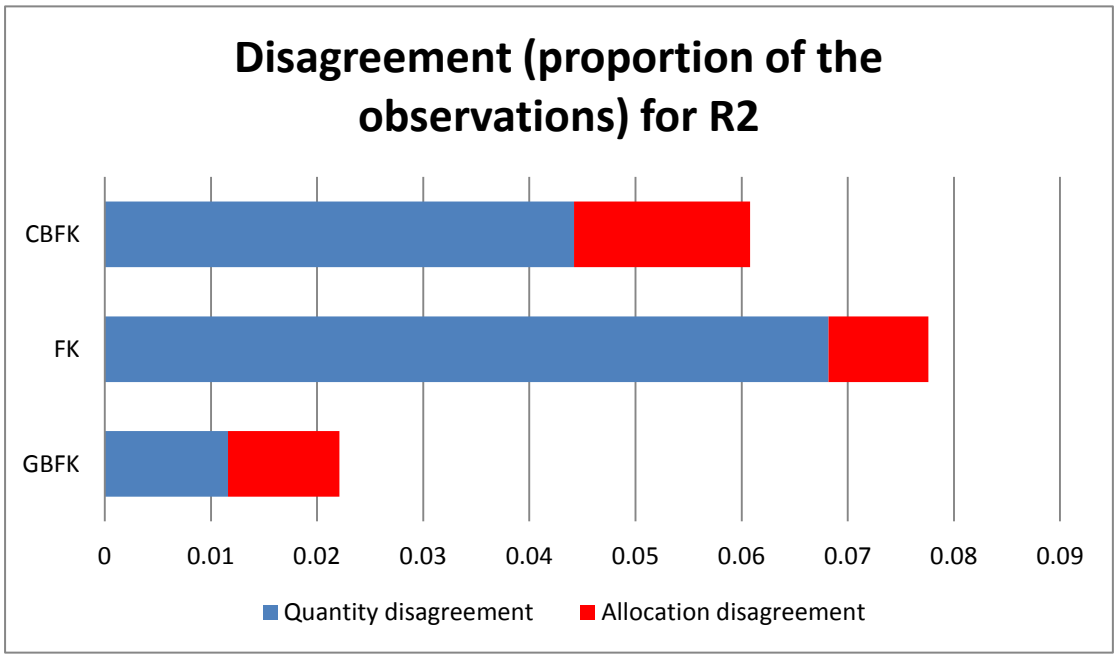

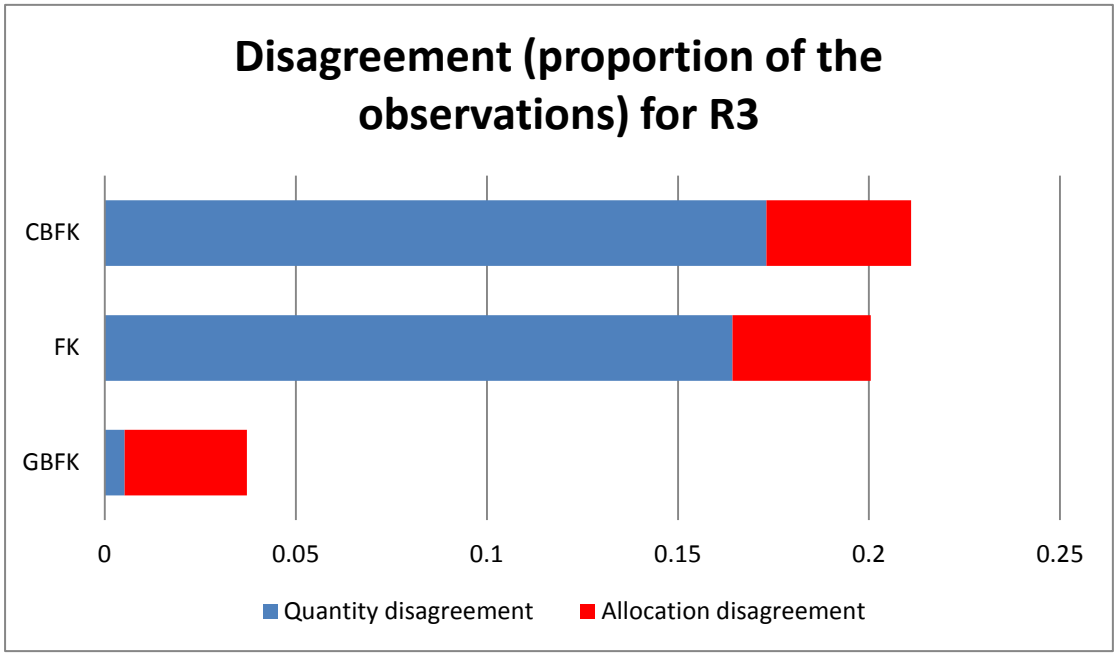

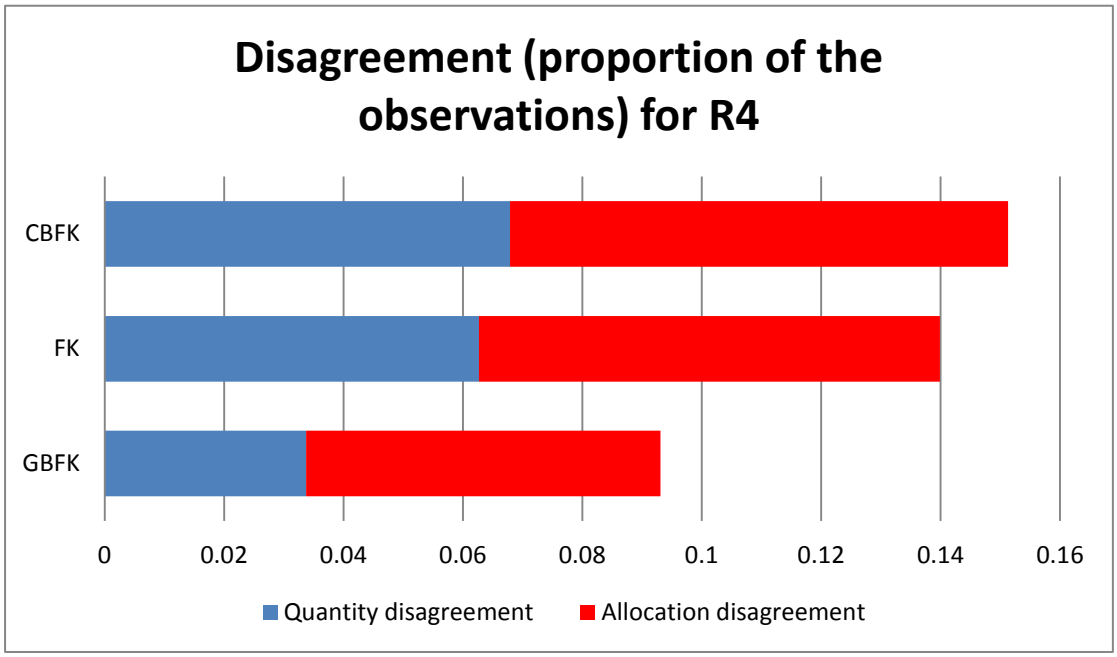

Fig. 5.13 Disagreement for R1, R2, R3 and R4 using GBFK, FK and CBFK

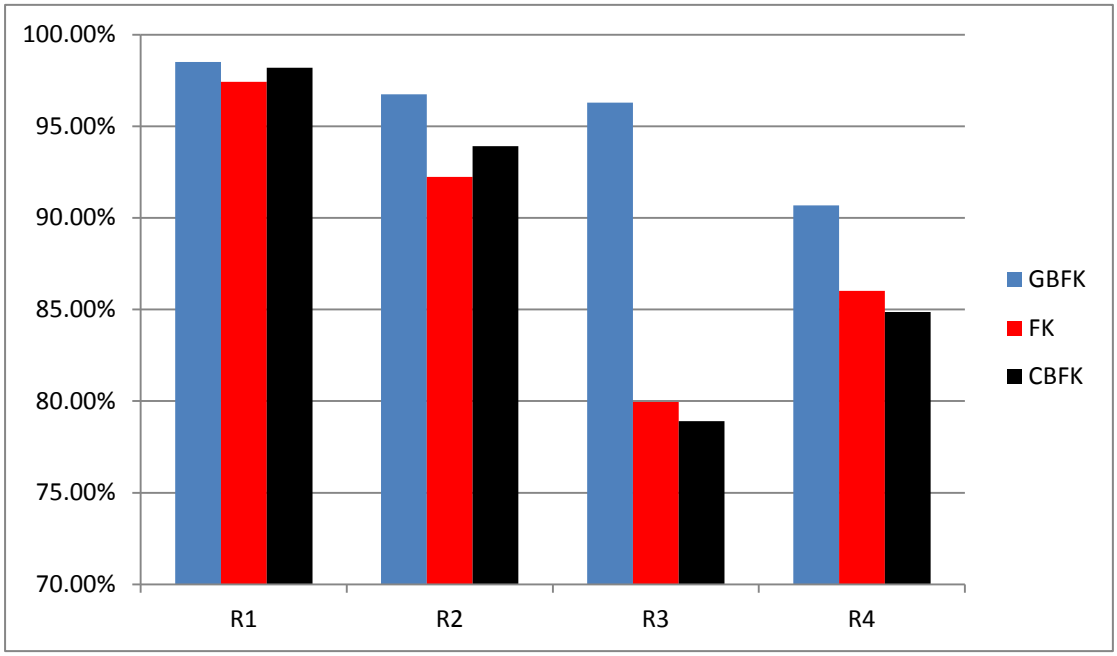

Fig. 5.14 Overall accuracy for R1, R2, R3 and R4 using GBFK, FK and CBFK.

All the algorithms were implemented under the MATLAB platform. All the computations were running on a laptop with an Inter(R) 2.40 GHZ Quad-Core processor. It took approximately 0.03, 4, 6, and 11 seconds, respectively for K-means, FK, CBFK and the proposed GBFK to process a 256×256 pixels SAR image.

Chapter 6

Conclusions and Recommendations

6.1 Summary

This thesis introduces a novel SAR sea-ice image segmentation approach named GBFK, which is based on the combination of the Gamma-based bilateral filter (GBF) and K-means clustering. In detail, this approach first employs a GBF in order to suppress the speckle noise. Since bilateral filter has proved to be a useful one that has the ability of smoothing while preserving edges, it is modified by taking spatial homogeneity into account and applying gamma distribution to describe the similarity of intensity. Then a K-means clustering algorithm is used as the second phase, followed by post-processing. As a pixel-based approach, GBFK achieved satisfactory performances in both simulated and real SAR data tests over several compared pixel-based approaches.

The main contributions of this thesis can be summarized as follows:

First, a novel approach for SAR sea-ice segmentation by adopting a new filter: bilateral filter (BF) was proposed. BF has low complexity and high computational efficiency. Consequently, it works well for SAR sea-ice image segmentation, and is

able to make a contribution to sea-ice detection.

Second, based on conventional BF, the spatial spread is made not a constant but adaptive to the local homogeneity. As a result, BF can effectively save more details when smoothing images in homogenous areas. In the meantime, an alternative function based on Gamma distribution is used to replace the original function of similarity of intensity in BF. It is obvious that Gamma function is more suitable for SAR sea-ice imagery than Gaussian function in this case. This improvement shows evident effectiveness according to the experimental results.

Third, quantitative evaluation shows that the proposed approach can achieve average overall accuracy of 95% when dealing with RADASAT-2 images in this study. Its results are approximately from 6.7% to 15.1% better than the comparative approaches, FK and CBFK, in terms of average overall accuracy. That means the proposed method is useful and promising on segmenting SAR imagery.

6.2 Recommendations

For automatic SAR sea-ice segmentation, although the proposed GBFK approach demonstrates promising results, several priorities for future research remain.

Firstly, although the local homogeneity was fully used in this approach, the texture

information was not employed. Since texture is considered to be critical for sea ice (Clausi, 1996), it could be useful to establish a model to adapt the parameter in BF accordingly using texture information. This is a way to improve the accuracy yet costing more processing time.

Secondly, like the replacement of similarity of intensity in BF, other model can be adopted as spatial closeness as well. For instance, Huang (2006) introduced a new model for spatial closeness and got a good effect on dealing with the impulse noise. In addition, new model can also be created for spatial closeness in BF based on properties of SAR sea-ice imagery.

Thirdly, the modifications in our approach focus on the performance or accuracy of the results, so the computational time is put on the secondary stage. Since some researcher have come up with ideas to accelerate the BF (Chaudhury et al., 2011; Weiss, 2006; Durand and Dorsey, 2002), their methods can be incorporated to the GBFK approach in order to achieve better time cost.

Finally, although the K-means clustering is used to underline the filtering phase, K-means is exactly too simple to be used in the clustering phase. It is worth to try other clustering methods such as GMM or KIF mentioned in the Chapter 2. Particularly in my opinion, fuzzy C-means algorithm can become a useful one for SAR sea-ice segmentation, because in fact, the boundaries between different ice types

are fuzzy, and even not easy to be distinguished by human (i.e. in Fig. 4.12, the boundaries between gray ice and first-year ice are difficult to be drawn for R4). Therefore, a fuzzy approach probably can achieve better results.

References

Alf M., Nieddu L., & Vicari D. (2008). A finite mixture model for image segmentation. *Stat Comput.*, Vol. 18, pp. 137-150.

Archer, D., & Bufett, B. (2005). Time-dependent response of the global ocean clathrate reservoir to climatic and anthropogenic forcing. *Geochemistry Geophysics Geosystems,* 6 (3): Q03002.

Benboudjema, D., Tupin, F., Pieczynski, W., Sigelle, M., & Nicolas, J.-M. (2007). Unsupervised segmentation of SAR images using Triplet Markov fields and Fisher noise distributions. *IGARSS 07*, July 23-28, 2007, Barcelona, Spain, 3891-3894.

Buades, A., Coll, B., & Morel, J.-M. (2006). The staircasing effect in neighborhood filters and its solution. *IEEE Transactions on Image Processing*, 15(6): 1499-1505.

Canadian Ice Service (CIS). (2012). Interpreting Ice Charts [Online]. Available: http://www.ec.gc.ca/glaces-ice/default.asp?lang=En&n=D5F7EA14-1&offset=1&toc=show.

Canadian Space Agency (CSA). (2011). RADARSAT Systems: Satellite Characteristics [Online]. Available: http://www.asc-csa.gc.ca/eng/satellites/radarsat/radarsat-tableau.asp

Carsey, F.D., Barry, R.G., & Weeks, W.F. (1991). *Chapter 1: Introduction. In F.D. Carsey (Ed.)*, Microwave Remote Sensing of Sea Ice, AGU Geophysical

Monograph 68, pp. 1-7. Washington: American Geophysical Union.

Casey, J. A.. (2010). *Dual-polarization (HH/HV) RADARSAT-2 ScanSAR Observations of New, Young and First- year Sea Ice*. M.Sc. Thesis, University of Waterloo, Canada.

Chaudhury, K. N., Sage, D., & Unser, M. (2011). Fast O(1) bilateral filtering using trigonometric range kernels. *IEEE Transactions on Image Processing*, 20(12): 3376-3382.

Choudhury, P., & Tumblin, J. (2003). The trilateral filter for high contrast images and meshes, In *Proceedings of the Eurographics Symposium on Rendering*, pp. 1-11.

Clausi, D. A. (1996). *Texture Segmentation of SAR Sea Ice Imagery*. Ph.D. Thesis, University of Waterloo, Canada.

Clausi, D. A., Qin, A. K., Chowdhury, M. S., Yu, P., and Maillard, P. (2010). MAGIC: MAp-Guided Ice Classification System. *Can. J. Remote Sensing*, Vol. 36, Suppl. 1, pp. S13–S25.

Clausi, D. A. and Yue, B. (2004). Comparing Cooccurrence Probabilities and Markov Random Fields for Texture Analysis of SAR Sea Ice Imagery. *IEEE Transactions on Geoscience and Remote Sensing*, 42(1): 215-228.

Deng, H., & Clausi, D. A. (2005). Unsupervised Segmentation of Synthetic Aperture Radar Sea Ice Imagery Using a Novel Markov Random Field Model. *IEEE Transactions on Geoscience and Remote Sensing*, 43(3): 528-538.

Deser, C., Walsh, J. E., & Timlin, M. S. (2000). Arctic Sea Ice Variability in the

Context of Recent Atmospheric Circulation Trends. *J. Climate,* 13(3): 617–633.

Durand, F., & Dorsey, J. (2002). Fast bilateral filtering for the display of highdynamic- range images. In *Proceedings of ACM Transactions on Graphics,* 21(3): 257–266.

Eisenman, I., & Wettlaufer, J.S. (2009). Nonlinear threshold behavior during the loss of Arctic sea ice. In *Proceedings of the National Academy of Sciences of the United States of America,* 106 (1): 28–32.

Elad, M. (2002). On the Origin of the Bilateral Filter and Ways to Improve It. *IEEE Transactions on Image Processing*, 11(10): 1141-1151.

Frost, V., Stiles J., Shanmugan, K., & Holtzman, J. (1982). A model for radar images and its application to adaptive digital filtering of multiplicative noise. *IEEE Trans. Pattern Anal. Mach. Intell*., PAMI-4(2): 157-166.

Gagnon, L., & Jouan, A. (1997). Speckle Filtering of SAR Images - A Comparative Study Between Complex-Wavelet-Based and Standard Filters. In *Proceedings of Wavelet Applications in Signal and Image Processing V*, San Diego, pp. 80-687.

Goodman, J. W. (1976). Some fundamental properties of speckle. *J. Opt. Soc. Amer.*, Vol. 66, pp. 1145-1150.

Hallikainen, M., & Winebrenner, D. P. (1992). *Chapter 3: The Physical Basis for Sea Ice Remote Sensing.* In *F.D. Carsey (Ed.)*. Microwave Remote Sensing of Sea Ice, AGU Geophysical Monograph 68, pp. 29-45. Washington: American Geophysical Union.

Hartigan, J. A., & Wong, M. A. (1979). A K-Means Clustering Algorithm. *Journal of the Royal Statistical Society*. *Series C (Applied Statistics)*, 28(1): 100-108.

Haverkamp, D., Soh, L. K., & Tsatsoulis, C. (1993). A dynamic local thresholding technique for sea ice classification. *Proc. IGARSS*, Vol. 2, pp. 638-640.

Herrera, J. V. M. (2005). Code: K-means image segmentation [Online]. Available: http://www.mathworks.com/matlabcentral/fileexchange/8379-kmeans-image-segmentation/content/kmeans.m.

Hu, Xiangyun, Tao, C. Vincent, & Prenzel, Björn. (2005). Automatic segmentation of high-resolution satellite imagery by integrating texture, intensity, and colour features. *Photogrammetric Engineering & Remote Sensing*, 71 (12): 1399-1406.

Huang Y. L., & Fuh C. S. (2006). Noise reduction using enhanced bilateral filter. *Images and Recognition*, 12(4):46-53.

IARC-JAXA. (2012). Arctic Sea Ice Extent [Online]. Available: http://www.ijis.iarc.uaf.edu/en/home/seaice_extent.htm.

Jacobs, D. D. (2010). Baltic Sea ice strands thousands of ferry passengers [Online]. Available: http://www.examiner.com/article/baltic-sea-ice-strands-thousands-of-ferry-passengers.

Jobanputra, R. (2004). *Preserving Texture Boundaries for SAR Sea Ice Segmentation*. M.Sc. Thesis, University of Waterloo, Canada.

Jobanputra, R., & Clausi, D. A. (2006). Preserving boundaries for image texture segmentation using grey level co-occurring probabilities. *Pattern Recognition*

Vol. 39, pp. 234-245.

Jr, R. G. P., & Millones, M. (2011). Death to Kappa: birth of quantity disagreement and allocation disagreement for accuracy assessment. *International Journal of Remote Sensing*, 32(15): 4407-4429.

Karvonen, J. (2010). C-Band Sea Ice SAR Classification Based on Segmentwise Edge Features. *Geoscience and Remote Sensing, New Achievements*, pp: 129-146.

Karvonen, J. A. (2004). Baltic Sea ice SAR segmentation and classification using modified pulse-coupled neural networks. *IEEE Transactions on Geoscience and Remote Sensing*, 42(7): 1566 – 1574.

Kuan, D., Sawchuk, A., Strand, T., & Chavel, P. (1987). Adaptive restoration of images with speckle. *IEEE Trans. Acoust., Speech, Signal Process.*, ASSP-35(3): 373-383.

Kwon, T-.J. (2012). ETVOS: An Enhanced Total Variation Optimization Segmentation Approach for SAR Sea-Ice Image Segmentation. *IEEE Transactions on Geoscience and Remote Sensing*, doi:10.1109/TGRS.2012.2205259

Lee, J. S. (1980). Digital image enhancement and noise filtering by use of local statistics. *IEEE Transactions on Pattern Analysis and Machine Intelligence,* PAMI-2(2): 165-168.

Leeuw, M. R., & Carvalho, L. M. T. (2009). Performance evaluation of several adaptive speckle filters for SAR imaging. *Anais XIV Simpósio Brasileiro de Sensoriamento Remoto*, Natal, Brasil, INPE, pp. 7299-7305.

Li, G., & Yu, W. (2012). SAR Image Despeckling Based on Adaptive Bilateral Filter. *Journal of Electronics and Information Technology*, 34(5): 1076-1081.

Lillesand, T. M., & Kiefer, R. W. (1987). *Remote Sensing and Image Interpretation (2nd edition)*. John Wiley and Sons, Toronto.

Lopes, A., Touzi R., & Nezry E. (1990). Adaptive Speckle Filters and Scene Heterogeneity. *IEEE Transactions on Geoscience and Remote Sensing*, 28(6): 992-1000.

Lopes, A., Nezry, E., Touzi, R., & Laur, H. (1993). Structure Detection and Statiscal Adaptive Speckle Filtering in SAR Images", *Int. J. Remote Sensing*, Vol. 14, pp. 1735-1758.

Lu, B., & Ku, Y. (2010). Speckle Reduction with Multiresolution Bilateral Filtering for SAR Image, In *Machine Vision and Human-Machine Interface (MVHI), 2010 International Conference*, April 24-25, 2010, Kaifeng, China, 700-703.

Marques, R. C. P., Carvalho, E. A., Costa, R. C. S., & Medeiros, F. N. S. (2004). Filtering effects on SAR images segmentation. *Lecture Notes in Computer Science*, Vol. 3124, pp. 1041-1046.

Molina, D E, Gleich, D, & Datcu, M. (2010). Gibbs random field models for model-based despeckling of SAR images. *IEEE Geoscience and Remote Sensing Letters*, 7(1): 73-77.

Oliver, C., & Quegan, S. (1998). *Understanding Synthetic Aperture Radar Images*. Boston. Artech House, pp. 75-120.

Otsu, N. (1979). A threshold selection method from grey-level histogram. *IEEE Trans.*

Systems, Man, and Cybernetics, Vol. 9, pp. 62-66.

Paris, S., Kornprobst, P., Tumblin, J., & Durand, F. (2009). Bilateral Filtering: Theory and Applications. *Foundations and Trends R in Computer Graphics and Vision*, 4(1): 1-73.

Perona, P., & Malik, J. (1990). Scale space and edge detection using anisotropic diffusion. *IEEE Transactions on Pattern Analysis and Machine Intelligence*, 12(7): 629-639.

Pianykh, O. S. (2010). Bilateral filters: what they can and cannot do. *Computer Vision and Pattern Recognition (cs.CV)*, arXiv:1007.1016.

Rijsbergen, C. J. van. (1979). *Information Retrieval (2nd ed.)*. Woburn. MA: Butterworth-Heinemann.

Rocha, R. F. (2008). Use of statistical distribution for segmentation of SAR images of oceanic areas. Remote Sensing Division, Hydrographic Navy Center, Av. Barão de Jaceguay s/n, 24048-900.

Samadani, R. (1995). A finite mixtures algorithm for finding proportions in SAR images. *IEEE Transactions on Image Processing*, 4(8): 1182-1185.

Sandven, S., & Johannessen, O. M. (2006). *Sea Ice Monitoring by Remote Sensing*. Encyclopedia of Analytical Chemistry.

Serreze, M. C., Barrett, A. P., Stroeve, J. C., Kindig, D. N., & Holland, M. M. (2009). The emergence of surface-based Arctic amplification. *The Cryosphere*, 3, 11-19.

Satellite Imaging Corporation (SIC). (2012). ASTER SATELLITE SENSOR [Online].

Available: http://www.satimagingcorp.com/satellite-sensors/aster.html.

Soh, L., & Tsatsoulis, C. (1999). Texture Analysis of SAR Sea Ice Imagery Using Gray Level Co-Occurrence Matrices. *IEEE Transactions on Geoscience and Remote Sensing*, 37(2): 780-795.

Soh, L., Tsatsoulis, C., Gineris, D., & Bertoia, C. (2004). ARKTOS: An Intelligent System for SAR Sea Ice Image Classification. *IEEE Transactions on Geoscience and Remote Sensing*, 42(1): 229-248.

Stern, H. L., & Moritz, R. E. (2000). Sea Ice Kinematics and Surface Properties from RADARSAT SAR During the SHEBA Drift. *Journal of Geophysical Research*, V. 107, 8028, 10 pp.

Tomasi, C., & Manduchi, R. (1998). Bilateral Filtering for Gray and Color Images, In *Sixth International Conference on Computer Vision*, Jan. 4-7, 1998, Bombay, India, 839-846.

Touzi, R. (2002). Review of Speckle Filtering in the Context of Estimation Theory. *IEEE Transactions on Geoscience and Remote Sensing*, 40(11): 2392-2404.

Tran, T. N., Wehrens, R., Hoekman, D. H., & L. Buydens, M. C.. (2005). Initialization of Markov random field clustering of large remote sensing images. *IEEE Transactions on Geoscience and Remote Sensing*, 43(8): 321-344.

Touzi, R. (2002). A review of speckle filtering in the context of estimation theory. *IEEE Trans. Geosci. Remote Sens.,* 40(11): 2392–2404.

Wackerman, C., Jentz, R., and Shuchman, R. (1988). *Present Status of SAR Sea Ice Algorithms*. ERIM. 33p. Report No.: ERIM-269600-14-T.

Walessa, M. and Datcu, M. (2000). Model-Based Despeckling and Information Extraction from SAR Images. *IEEE Transactions on Geoscience and Remote Sensing*, 38(5): 2818 - 2835.

Weisenseel, R. A., Karl, W. C., Castanon, D. A., Power, G. J., & Douville, P. (1999). Markov random field segmentation methods for SAR target chips. In *Proceedings of Algorithms for Synthetic Aperture Radar Imagery VI*, E.G. Zelnio, editor, Proc. SPIE V 3721, Orlando, Florida.

Weiss, B. (2006). Fast median and bilateral filtering. *ACM Transactions on Graphics (TOG)*, 25(3): 519 - 526,.

Wong, A., Zhang, W., and Clausi, D. A. (2009). IceSynth: An image synthesis system for sea-ice segmentation evaluation. In *2009 Canadian Conference on Computer and Robot Vision,* May 25-27, 2009, Kelowna, BC, 178-183.

Wong, A., Yu, P., Zhang, W., & Clausi, D. A. (2010). IceSynth II: Synthesis of SAR Sea-Ice Imagery Using Region-Based Posterior Sampling. *IEEE Geoscience and Remote Sensing Letters*, 7(2): 348-351.

Descombes, X., Morris, R., Zerubia, J., & Berthod, M. (1996). Estimation of Markov Random Field prior parameters using Markov chain Monte Carlo Maximum Likelihood. *IEEE Transactions on Image Processing*, 8(7): 954-963.

Yang, X., & Clausi, D. A. (2007). SAR Sea Ice Image Segmentation Based on Edge-preserving Watersheds. In *4th Annual Canadian Conference on Computer and Robot Vision*, May 28-30, 2007, Montreal, Quebec, 426-431.

Yang, X., & Clausi, D. A. (2009). SAR sea ice image segmentation using an

edge-preserving region-based MRF. In *International Conference on Image Processing (ICIP)*, Cairo, Egypt, Nov 7-11.

Yu, P. (2009). *Segmentation of RADARSAT-2 Dual-Polarization Sea Ice Imagery*. M.Sc. Thesis, University of Waterloo, Canada.

Yu, P., Clausi, D. A., & Howell, S. E. L. (2009). Fusing AMSR-E and QuikSCAT Imagery for Improved Sea Ice Recognition. *IEEE Transactions on Image Processing*, 47(7): 1980-1989.

Yu, Q., & Clausi, D. A. (2006). IRGS: Image Segmentation Using Edge Penalties and Region Growing. *IEEE Transactions on Image Processing*, 30(12): 2126-2139.

Yu, Q., & Clausi, D. A. (2007). SAR Sea-Ice Image Analysis Based on Iterative Region Growing Using Semantics. *IEEE Transactions on Image Processing*, 45(12): 3919-3931.

Yu, Q., & Clausi, D. A. (2006). Filament Preserving Model (FPM) Segmentation Applied to SAR Sea-Ice Imagery. *IEEE Transactions on Image Processing*, 44(12): 3687-3694.

Zhang, M., & Gunturk, B. K. (2008). Multiresolution Bilateral Filtering for Image Denoising. *IEEE Transactions on Image Processing*, 17(12): 2324-2333.

Zhang, W. G., Liu, F., & Jiao, L. C. (2009). SAR image despeckling via bilateral filtering. *Electronics Letters*, 45(15): 781-783.